https://doi.org/10.5194/egusphere-2026-6912
Preprint. Discussion started: 12 November 2026
© Author(s) 2026. CC BY 4.0 License.

Circulation, mixing, and biogeochemical exchange in the Gulf of Taranto

Malek Belgacem[1,2*], Florian V. M. Kokoszka[1*], Carolina Cantoni[1], Katrin Schroeder[1], Jacopo Chiggiato[1], Stefania Sparnocchia[1], Elena Fragiacomo[1], Francesco Acri [1], Marzia Rovere[1]

[1]Consiglio Nazionale delle Ricerche-Istituto di Scienze Marine (CNR-ISMAR), Venice/Naples/Trieste/Bologna, Italy
[2]International Ocean Carbon Coordination Project (IOCCP), Institute of Oceanology, Polish Academy of Sciences, Sopot, Poland

Correspondence to: Malek Belgacem (malekbelgacem@cnr.it)

[*]authors contributed equally

Abstract. The Gulf of Taranto, between the Adriatic and eastern Mediterranean basins, is a gateway for water-mass exchange and transformation, yet its vertical mixing and the biogeochemical consequences remain poorly quantified. We present a full-depth transect across the Gulf entrance, sampled during the PIONEER-2023 cruise (November–December 2023), combining hydrography and velocity with dissolved oxygen, nutrients, dissolved inorganic carbon and total alkalinity. The section was occupied in a cyclonic state, with doming isopycnals in the upper 300 m lifting nutrient- and carbon-rich water. Water-mass-resolved transports describe an asymmetric but compensated exchange: a robust eastern surface inflow, a weaker, marginally resolved resident deep inflow, and an Adriatic-derived deep vein entering and leaving without a resolvable net contribution. Section-integrated budgets are indistinguishable from zero for every tracer, so the result is how exchange partitions among water masses, not a net budget. Finescale estimates reveal contrasting regimes around an oxygen minimum layer near 1000 m: double-diffusive above, internal-wave-driven below and in deeper sheared layers. Oxygen, dissolved inorganic carbon and alkalinity converge into the layer across both boundaries, preferentially from below, whereas nutrient fluxes are tracer-specific, phosphate and silicic acid differing in direction from nitrate. Because diapycnal exchange supplies oxygen from both sides, it erodes the minimum rather than sustaining it; its persistence requires consumption or advective terms a single survey cannot resolve. The Gulf thus acts as an active transformation zone rather than a passive conduit, modifying the ventilation state, nutrient content and carbonate chemistry of the water masses crossing it toward the Ionian Sea.

1 Introduction

The Gulf of Taranto (Fig. 1a), located in the northern Ionian Sea, is a key transition zone between the Adriatic Sea and the Eastern Mediterranean basin. Its hydrographic and biogeochemical structure reflects the interaction of multiple water masses under the combined influence of regional circulation, steep topography, and air-sea forcing. Previous studies have shown that the Gulf is characterized by basin-scale gyre variability, mesoscale to submesoscale circulation, and strong exchange with the northern Ionian Sea (Pinardi et al., 2016; Trotta et al., 2017; Federico et al., 2020). Despite its strategic position, the Gulf

https://doi.org/10.5194/egusphere-2026-6912
Preprint. Discussion started: 12 November 2026
© Author(s) 2026. CC BY 4.0 License.

remains poorly characterized with respect to vertical mixing processes and their biogeochemical consequences, particularly in the intermediate and deep layers (Sellschopp and Onken, 2000; Sellschopp and Álvarez, 2003). Sellschopp and Álvarez (2003) showed the steep shelf slope of the Gulf transforms the dense coastal water leaving the Adriatic through intrusion and mixing with ambient water. The transformed product occupies a broad depth interval on the western slope of the Ionian Sea and may be the origin of cold lenses observed below the thermocline in the central Ionian Sea (Sellschopp and Onken, 2000). The Gulf therefore acts as pathways but as a site of dense-water modification, the process our transect is positioned to sample.

At the regional scale, the Ionian Sea is a major crossroads of Mediterranean water masses with contrasting origins and properties. In the upper layer, relatively low-salinity Atlantic-derived waters (AW) enter from the Western Mediterranean and are progressively modified along their eastward pathway (Roether et al., 1996; Schroeder et al., 2024).

At intermediate depths, Levantine Intermediate Water (LIW) and Cretan Intermediate Water (CIW), collectively referred to here as Eastern Intermediate Water (EIW) and Eastern Intermediate Water core (EIW-core), spread westward from the Eastern Mediterranean (Roether et al., 1996; Schroeder et al., 2024). The deeper layers are episodically renewed by Adriatic-derived Eastern Mediterranean Deep Water (EMDW-ad), formed through dense-water formation in the southern Adriatic and its subsequent intrusion into the Ionian abyssal layers (Manca et al., 2006; Rubino et al., 2012; Budillon et al., 2010).

The relative influence of these water masses is further modulated by the Adriatic-Ionian Bimodal Oscillating System (BiOS), a quasi-decadal alternation between cyclonic and anticyclonic circulation states that modifies the exchange between Adriatic and Levantine waters (Borzelli et al., 2009; Civitarese et al., 2010). The circulation state of the northern Ionian at the time of sampling therefore sets the context in which any single full-depth view of the Gulf must be interpreted.

The recent thermohaline history of the region adds further complexity. During the Eastern Mediterranean Transient (EMT) in the 1990s, the main source of EMDW shifted from the Adriatic to the Aegean Sea, producing anomalously warm and saline deep waters that propagated through the basin (Roether et al., 1996; Theocharis et al., 2002). Since the late 1990s, the Adriatic has resumed its role as a major deep-water source, although newly formed deep waters remain warmer and saltier than before the EMT (Theocharis et al., 2002; Roether et al., 2007; Manca et al., 2006). More recent observations indicate rapid warming and salinization of intermediate and deep waters in the Adriatic-Ionian region, suggesting ongoing changes in the preconditioning of dense-water formation, intermediate-water ventilation, and deep-water renewal (Terzić et al., 2025; Terzić and Vilibić, 2026; Menna et al., 2026). These changes are directly relevant to the Gulf of Taranto because it lies along the exchange pathway between EMDW-ad and the northern Ionian Sea.

Within this broader setting, the Gulf of Taranto acts as a mixing and exchange node where surface, intermediate, and deep waters converge over short horizontal scales. Surface and intermediate inflows interact with resident deep waters and EMDW-ad intrusions, generating strong vertical and lateral gradients in temperature, salinity, oxygen, nutrients, and carbonate-system variables. The complex morphology of the Gulf, including steep slopes, canyon systems, and deep structural depressions, may

https://doi.org/10.5194/egusphere-2026-6912
Preprint. Discussion started: 12 November 2026
© Author(s) 2026. CC BY 4.0 License.

favour boundary-layer turbulence, internal-wave activity, and localized exchange (Ceramicola et al., 2024; Musgrave et al., 2022). At the same time, within the ultra-oligotrophic Eastern Mediterranean, local processes such as cyclonic uplift, lateral advection, internal-wave mixing, and double-diffusive exchange may substantially influence nutrient supply to the upper ocean and the redistribution of oxygen and carbon within the interior (D'Ortenzio and Ribera d'Alcalà, 2009; Kunze et al., 2006; Zhang et al., 1998; Nakano and Yoshida, 2019). However, the intensity, spatial organization, and biogeochemical effects of these processes remain poorly quantified in the Gulf of Taranto.

The present study is based on observations collected during the PIONEER-2023 cruise (Processes in the Ionian Sea: Exploring, Experimenting, Researching), a multidisciplinary experiment carried out aboard the R/V Gaia Blu of the Italian National Research Council (CNR) between 17 November and 9 December 2023 (Rovere et al., 2024). The campaign covered the Ionian Sea and the Gulf of Taranto and combined physical, biogeochemical, geological, and optical observations. Here, we focus specifically on the full-depth transect across the entrance of the Gulf of Taranto to investigate the coupling between circulation, vertical mixing, and biogeochemical tracer distributions during the winter 2023 circulation regime. We analyse temperature, salinity, velocity, dissolved oxygen, nutrients, dissolved inorganic carbon, and total alkalinity in relation to water-mass structure, cyclonic circulation, isopycnal doming, and thermohaline layering. By combining water-mass analysis, section transport estimates, and parameterized vertical diffusivity and tracer fluxes, we assess how internal-wave mixing, double-diffusive structure, and deep-water intrusions contribute to nutrient redistribution, to the diapycnal oxygen budget of the Oxygen Minimum Layer (OML), and to exchange between the Gulf and the northern Ionian Sea.

2 Materials and methods

2.1 Study area

The Gulf of Taranto is a broadly square embayment bounded to the west by the Calabrian coast and to the east by the Apulian coast, connected to the open Ionian Sea by a wide, deep, triangular channel with maximum depths reaching approximately 2800 m in the south (Ceramicola et al., 2024). Its steep continental margins and submarine canyons are expected to favour internal-wave activity and boundary-layer exchange. The transect sampled here (11 stations, Fig. 1a, red dots) intersects the full width of the Gulf at its connection with the open Ionian Sea and was designed to capture the main inflow and outflow pathways of surface, intermediate, and deep waters.

2.2 Sampling and analytical procedures

Full details of the sampling programme, shipboard procedures and instrument calibration are given in the cruise report (Rovere et al., 2024); only the elements bearing directly on this analysis are summarized here. Conductivity, temperature, and dissolved oxygen were measured from surface to bottom with duplicate sensors on an SBE 911plus CTD mounted on a rosette carrying

https://doi.org/10.5194/egusphere-2026-6912
Preprint. Discussion started: 12 November 2026
© Author(s) 2026. CC BY 4.0 License.

12 Niskin bottles (12 L each) and binned to 1 dbar. Oxygen sensor data were post-calibrated against shipboard Winkler titrations, and bottle salinities were verified on board with an Autosal salinometer. Velocity profiles were obtained at every transect station with a dual-head lowered acoustic Doppler current profiler, with downward- and upward-looking heads mounted on the rosette carousel. On each upcast, water samples were drawn at up to 17 standard depths between 5 m and the seabed for nutrients (nitrate, phosphate and silicic acid) and for carbonate-system variables (TA and pH). Nutrient samples were stored frozen at −20 °C; samples for pH and TA were collected in 300 mL borosilicate bottles, poisoned with saturated $HgCl_2$ and sealed against gas exchange following Dickson et al. (2007).

2.2.1 Analytical methods

Nutrients were determined at the CNR-ISMAR Venice laboratory by standard colorimetry (Grasshoff et al., 1999; Hansen and Koroleff, 1999). Carbonate-system variables were analysed within 8 months at the CNR-ISMAR Trieste laboratory. pH was measured spectrophotometrically at 25.00 ± 0.1 °C with purified m-cresol purple (Liu et al., 2011) and is reported on the total scale; reproducibility on duplicates was ± 0.002 units and the measurement uncertainty ± 0.005 units, assessed against certified TRIS buffer. TA was determined by open-cell potentiometric titration with a difference derivative readout (Hernández-Ayón et al., 1999), the titrant being standardized daily against certified reference material (batch 206) and yielding a mean offset of +0.6 µmol kg^{-1} and a precision of ± 2.22 µmol kg^{-1}. DIC was not measured directly but calculated from pH_T and TA with CO2SYS (van Heuven et al., 2011; Lewis and Wallace, 1998), using the dissociation constants of Lueker et al. (2000) for K_1 and K_2, Dickson (1990) for $KHSO_4$, Pérez and Fraga (1987) for KHF, and the borate ratio of Uppström (1974). Its overall uncertainty is ± 7.7 µmol kg^{-1}, and because it derives from pH and TA it is not independent of TA.

2.2.2 Physical and biogeochemical data integration

Velocities from the two LADCPs were post-processed with the LDEO_IX software in combination with the processed CTD data; further detail on data collection and processing during the 2023 cruise is given in the cruise report (Rovere et al., 2024). The processed velocity profiles were output on a 10 m vertical grid and then interpolated onto the 1 m CTD grid so that velocity and hydrography share a common vertical coordinate. Because interpolation adds no information, only velocity variations at vertical scales larger than the native 10 m LADCP spacing are treated as resolved, and finer structure in the merged profiles is not interpreted. Along-section and cross-section components were then obtained by rotating the zonal and meridional components onto the section heading, 38.95° relative to east, with positive cross-section velocity directed into the Gulf. The transport integrals described below are evaluated on this 1 m grid. Conservative Temperature (CT), Absolute Salinity (SA), the potential-density anomaly referenced to 0 dbar (σ_0), spiciness and the Turner angle (Turner, 1973) were computed with the Gibbs SeaWater (GSW) Oceanographic Toolbox implementing TEOS-10 (Python gsw v3.4.0; McDougall and Barker, 2011). Vertical sections of the CTD and discrete-bottle variables were produced by objective mapping (Bretherton et al., 1976; Hiller and Käse, 1983; Davis, 1985; Wunsch, 1996; Emery and Thomson, 1997), implemented as optimal interpolation (Liebelt,

https://doi.org/10.5194/egusphere-2026-6912
Preprint. Discussion started: 12 November 2026
© Author(s) 2026. CC BY 4.0 License.

1967; Gelb, 1974; Kamen and Su, 1999). The mapped fields are returned on a regular grid with a uniform vertical spacing of 10 m (229 levels, 0–2280 m) and a horizontal spacing of 0.0142° (80 nodes). This mapped grid is used for the section figures; the water-mass classification, the transport budgets and the diffusive fluxes are all computed on the 1 m profile grid described above. Apparent oxygen utilization was defined as AOU = O_2sat − O_2obs, where O_2sat is the oxygen solubility computed from CT, SA, and pressure (GSW O2sol) and O_2obs is the measured concentration. AOU is interpreted as the oxygen deficit relative to saturation rather than as a local respiration rate, because it may include preformed air–sea disequilibrium and subsequent mixing.

2.3 Wind stress and sea level height

Sea level anomalies and absolute surface geostrophic currents were taken from the Copernicus Marine Service altimeter product (https://doi.org/10.48670/moi-00142), referenced to a 1993–2012 mean. Wind stress was taken from the global hourly sea-surface wind and stress product derived from scatterometer data and model output (https://doi.org/10.48670/moi-00305).

2.4 Parameterized vertical diffusivity

Two finescale approaches were used to describe potential vertical exchange below the surface mixed layer. Both are indirect, and are used to compare the spatial organization of mixing regimes rather than as substitutes for direct microstructure measurements.

Internal-wave-driven mixing (IW). The turbulent kinetic energy dissipation rate was estimated from the shear–strain finescale parameterization (Gregg, 1989; Polzin et al., 1995; Kunze et al., 2006; Ferron et al., 2014; Polzin et al., 2014; Kokoszka et al., 2026) as

$$\varepsilon_{iw} = \varepsilon_0 (N/N_0)^2 \ (E/E_{GM})^2 F(R_\omega) L(f,N) \quad (1)$$

where N is the local buoyancy frequency and E/E_{GM} is the observed internal-wave variance normalized by the Garrett–Munk reference variance, diagnosed either from the velocity shear (the vertical gradient of horizontal velocity) or from the isopycnal strain (the vertical gradient of isopycnal displacement, estimated from buoyancy-frequency anomalies relative to the background stratification). R_ω describes the frequency content of the internal-wave field through the buoyancy-normalized shear-to-strain variance ratio, and $F(R_\omega)$ and L(f,N) account for the wave-frequency distribution and the latitude dependence respectively. The shear- and strain-based forms of these functions follow Kunze et al. (2006). Reference values were $\varepsilon_0 = 7 \times 10^{-10}$ W kg^{-1} and $N_0 = 5.2 \times 10^{-3}$ rad s^{-1}. The corresponding diffusivity follows from the Osborn (1980) relation,

$$K_{iw} = \Gamma \varepsilon_{iw} / N^2 \quad (2)$$

https://doi.org/10.5194/egusphere-2026-6912
Preprint. Discussion started: 12 November 2026
© Author(s) 2026. CC BY 4.0 License.

with a mixing efficiency Γ = 0.2; a fuller presentation of the formulation is given by Kokoszka et al. (2026). Shear and strain spectra were computed over 320 m vertical segments mapped every 10 m and integrated over 320–80 m for shear and 107–10 m for strain, bands that retain the resolved finescale variance while excluding the noise-dominated parts of the LADCP and CTD spectra. No spectral saturation cutoff was applied, because in sensitivity tests it substantially reduced the effective shear bandwidth. Because the parameterization treats all resolved finescale shear as wave-borne, dissipation is overestimated wherever sub-inertial or geostrophic shear contributes at the same vertical scales (Takahashi and Hibiya, 2019). Finescale parameterizations may also exceed microstructure-derived dissipation by a factor of about 2–3, so the estimates were divided by three (Fine et al., 2021; Takahashi and Hibiya, 2021), and profiles were then averaged in 80 m bins. Two products are reported: K_ρ^{IW}, the shear-based estimate used in all flux calculations, and K_ρ^{IW*}, the strain-based estimate, retained only as a consistency check and not used quantitatively because its resolved band is narrower and noise-limited at small vertical scales.

Double-diffusive mixing (DD). Salt-fingering (SF) and diffusive-convective (DC) regimes were identified from the density ratio:

$$R_\rho = (\alpha \partial\vartheta/\partial z)/(\beta \partial S/\partial z) \qquad (3)$$

where α is the thermal expansion coefficient, β the haline contraction coefficient, and $\partial\theta/\partial z$ and $\partial S/\partial z$ the vertical gradients of Conservative Temperature and Absolute Salinity, computed after averaging profiles over 10 m. Layers with $1.0 < R_\rho < 3.0$ were classified as salt fingering and those with $0.5 < R_\rho < 1.0$ as diffusive convection, and continuous patches thinner than 5 m were discarded. To restrict the analysis to the most active regimes, only patches with R_ρ below the salt-fingering median of 1.41 or above the diffusive-convective median of 0.86 were retained, each patch being assigned a uniform classification over its full vertical extent. Temperature and salt diffusivities K_T and K_S were obtained from the formulations of Zhang et al. (1998), Radko and Smith (2012) and Nakano and Yoshida (2019) as synthesized by Kokoszka et al. (2021), without retuning their published coefficients. The density diffusivity for each regime is

$$K_\rho = (K_T R_\rho - K_S)/(R_\rho - 1) \quad (4)$$

and the two contributions are combined as

$$K_{\rho,dd} = K_{\rho,SF} + K_{\rho,DC} \qquad (5)$$

Because the two regimes occupy distinct R_ρ ranges, only one contributes at any depth, and the magnitude of the combined diffusivity is used in the flux calculations below. Equation (4) is singular as $R_\rho \rightarrow 1$, and the retention criteria adopted here keep the patches closest to unity. The symbols K_{iw} and $K_{\rho,dd}$ in Eqs. (2) and (5) are written K_ρ^{IW} and K_ρ^{DD} from here on.

2.5 Water-mass classes and tracer fluxes calculations

Throughout, we use a local classification into hydrographic-biogeochemical classes rather than unmixed source water masses. Ionian/Atlantic-derived surface water of Adriatic influence is separated into western (ISW/AW-w) and eastern (ISW/AW-e)

https://doi.org/10.5194/egusphere-2026-6912
Preprint. Discussion started: 12 November 2026
© Author(s) 2026. CC BY 4.0 License.

branches according to position along the section. Levantine and Cretan Intermediate Water are treated together as Eastern Intermediate Water (EIW-core), the intermediate salinity-maximum layer, and EIW-down denotes its weakly ventilated lower part. The oxygen minimum layer (OML) is the low-oxygen core within the transitional layer rather than a separate water mass. The deep layer comprises resident Eastern Mediterranean Deep Water (EMDW-r) and an Adriatic-derived intrusive vein (EMDW-ad).

The section was partitioned into seven hydrographic-biogeochemical classes; ISW/AW-w, ISW/AW-e, EIW-core, EIW-down, OML, EMDW-r, and EMDW-ad. Because the classes overlap in σ_0, in depth and in CT–SA space, they were assigned in the fixed priority order, so that each 1 m cell belongs to exactly one class. The density bounds reported under Water masses, binning, and interfaces of interest are therefore the ranges occupied by each class after assignment, not independent thresholds; in particular EMDW-ad ($\sigma_0 \geq 29.186$ kg m^{-3}) and EMDW-r ($\sigma_0 \geq 29.193$ kg m^{-3}) extend into the density band bounded by the OML interfaces, where they are separated from the OML by oxygen and by position along the section rather than by density. The classes were defined from σ_0, CT–SA structure, oxygen, spiciness, and location along the section. Throughout, u denotes the combined (propagated + bootstrap) standard uncertainty of an integrated flux or transport, and significance is quoted as the ratio $|F|/u$. A term is called robust when $|F| \geq 2\,u$, marginal when $u \leq |F| < 2u$, and not significant when $|F| < u$.

2.5.1 Horizontal advection of tracers

The horizontal transport through each grid point is computed as $T = C\ U\ dz\ L$ where C is the mass concentration to be transported, U the cross-section velocity, obtained by projecting the zonal (u) and meridional (v) velocity components onto the section heading, dz is the vertical bin thickness, taken as 1 m, and L is the horizontal distance between station midpoints (m). Virtual endpoints at (38.95°N, 17.10°E) and (39.75°N, 18.45°E) are used to define the lateral extent of the first and last stations to obtain L at the section borders. T is then summed within each water-mass bin to estimate layer-integrated horizontal budgets. For salinity (g kg^{-1}), the mass concentration is obtained by multiplying by in situ density (kg m^{-3}), yielding transports in g s^{-1}. Oxygen, nutrients, dissolved inorganic carbon and total alkalinity (μmol kg^{-1}), are similarly converted to μmol m^{-3} by multiplying by in situ density, yielding transports in μmol s^{-1}. Uncertainty in horizontal transports was estimated by combining prescribed local uncertainties in velocity and tracer concentrations with a station-resampling bootstrap. The propagated local uncertainty was computed from the transport equation by assuming independent uncertainties σ_C and σ_U in mass concentrations and cross velocities (respectively). This leads to $\delta T = \sqrt{\sum (U\sigma_C dz\ L)^2 + \sum (C\sigma_U dz\ L)^2}$. A bootstrap uncertainty was also estimated by resampling the station columns with replacement N = 300 times within each water-mass bin and recomputing the integrated transport for each realization. The final uncertainty was obtained as $\delta T_{total} = \sqrt{\delta T^2 + \delta T_{boot}{}^2}$. In practice, the propagated local uncertainty was typically only 2–11% of the bootstrap uncertainty, increasing the final combined uncertainty by less than about 1% in amplitude. Reported uncertainties therefore mainly reflect the sensitivity of the horizontal transport estimates to the spatial sampling of the section.

https://doi.org/10.5194/egusphere-2026-6912
Preprint. Discussion started: 12 November 2026
© Author(s) 2026. CC BY 4.0 License.

2.5.2 Diffusive vertical fluxes

Turbulent diffusivities associated with internal-wave mixing (K_{iw}) and double-diffusive mixing (K_{dd}) were used to compute vertical diffusive tracer fluxes across density-defined Interfaces of Interest (IOIs). Four IOIs are used. Three are centred on isopycnals separating vertically stacked classes: σ_0 = 29.120 kg m^{-3} (EIW-core–EIW-down), 29.184 kg m^{-3} (OML top, EIW-down–OML) and 29.195 kg m^{-3} (OML base, OML–EMDW-r). The fourth, σ_0 = 29.203 kg m^{-3}, lies within the EMDW domain, where EMDW-r and EMDW-ad are in lateral rather than density contact, and therefore quantifies diapycnal exchange within the deep layer rather than between the two deep classes. A vertical thickness of 160 m was used to compute diffusive fluxes. This choice is constrained by the effective resolution of the diffusivity estimates, which were derived from spectral calculations performed over 320 m segments and mapped every 10 m. A 160 m window centred on each isopycnal interface was adopted as a compromise between averaging a sufficient number of overlapping diffusivities estimates and retaining a localized representation of the interface. Sensitivity tests using window thicknesses between 80 and 240 m showed that the main flux patterns, including the sign and relative magnitude of the dominant fluxes across the OML and deep interfaces, remained unchanged (not shown), also supported by a test on spiciness, which indicated a smooth increase in within-window variability with increasing window thickness, consistent with the progressive inclusion of a larger fraction of the water column. Together, these tests support the choice of the adopted 160 m averaging scale for layer separation.

Before flux calculation, tracer concentrations were converted to volumetric units. Salinity, expressed in g kg^{-1}, was converted to g m^{-3} by multiplying by in situ density. Oxygen, nutrients, dissolved inorganic carbon and total alkalinity, expressed in μmol kg^{-1}, were converted to μmol m^{-3} using the same density conversion. With this convention, salinity fluxes are reported in g m^{-2} s^{-1}, while all chemical tracer fluxes are reported in μmol m^{-2} s^{-1}.

Discrete bottle data (dissolved inorganic carbon, total alkalinity and nutrients) were interpolated onto the 1 m profile grid before the window gradients were computed. Because standard bottle spacing below 500 m is 250 m, a 160 m window contains at most one discrete sample per station for these tracers; the gradient standard errors reported below therefore characterize the interpolated profiles rather than the discrete sampling. The significance of the bottle-derived fluxes in Table S1 should be read with that in mind. The salinity and oxygen fluxes derive from the 1 dbar CTD record and are not affected. Within each window, the vertical tracer gradient was estimated independently for each station by linear regression of tracer concentration against depth. The uncertainty on the gradient was taken as the standard error of the regression; in rare cases this value was not finite, and was approximated from the tracer standard deviation within the window divided by the vertical extent of the window. For each station and interface, the local flux was computed from the product between the mean diffusivity and the local vertical gradient using the Fick's law:

$$F = KdC/dz,$$

where z is depth (positive downward) and $\partial C/\partial z$ is the vertical mass-concentration gradient across the IOI. With this convention a positive F denotes an upward, down-gradient flux, equivalent to the usual form F = −K dC/dz' with z′ positive

https://doi.org/10.5194/egusphere-2026-6912
Preprint. Discussion started: 12 November 2026
© Author(s) 2026. CC BY 4.0 License.

upward. Internal-wave fluxes F_{iw} were computed using K_{iw}, while double-diffusive fluxes F_{dd} were computed using K_{dd}, with $K_{dd} = |K_{\rho,SF} + K_{\rho,DC}|$. The sign of the underlying double-diffusive density diffusivity reflects the net buoyancy effect of differential heat and salt transport, rather than the direction of transport of an arbitrary tracer. Its absolute value was therefore used as an effective exchange magnitude, while the direction of each tracer flux was determined by its local gradient and the adopted vertical sign convention. The two contributions F_{iw} and F_{dd} are retained separately before being summed. Uncertainty in the local diffusive flux was estimated by propagating the uncertainty in K and in dC/dz, assuming that the two terms are independent:

$$\delta F = |F|\sqrt{(\delta K/K)^2 + (\delta(dC/dz)/(dC/dz))^2}$$

where δK is the standard error of the mean diffusivity within the window, and $\delta(dC/dz)$ is the uncertainty on the vertical tracer gradient. For each IOI, fluxes were then integrated along the sampled section by summing the station contributions. Station fluxes were averaged along the sampled section to give a section-mean flux per unit interface area; the uncertainty associated with local flux estimates was combined in quadrature across stations and scaled accordingly. A second uncertainty term was estimated using a bootstrap approach. For each IOI and tracer, station fluxes along the section were resampled with replacement N = 300 times. The integrated flux was recomputed for each realization, and the bootstrap uncertainty was defined as the standard deviation of the resulting distribution. The final uncertainty on the section-integrated flux was obtained by combining the propagated local uncertainty and the bootstrap uncertainty in quadrature:

$$\delta F_{total} = \sqrt{\delta F^2 + \delta F_{boot}{}^2}.$$

Four limitations of this flux framework should be kept in mind. First, $|K_\rho^{DD}|$ is used as an effective exchange magnitude, so the estimate represents double-diffusive intensity and discards any signed or counter-gradient contribution; because the flux direction is then set by the local tracer gradient alone, all double-diffusive fluxes are down-gradient by construction. Second, a single effective double-diffusive diffusivity derived from the density flux is applied to all tracers, whereas for salt fingering the appropriate coefficient for a passive tracer is closer to K_S than to K_ρ (Inoue et al., 2007); the double-diffusive fluxes are therefore indicative in magnitude only. Third, KρIW is evaluated only within the double-diffusively active patches, so both components describe exchange within that sub-domain rather than across the whole water column; the contrast between internal-wave- and double-diffusion-dominated interfaces therefore also applies within it. Fourth, the internal-wave estimates assume that the resolved finescale shear is wave-borne; where the shear is sub-inertial, as in the deep jets described in the Results, the parameterization overestimates dissipation (Takahashi and Hibiya, 2019), and no spectral saturation cut-off was applied here.

https://doi.org/10.5194/egusphere-2026-6912
Preprint. Discussion started: 12 November 2026
© Author(s) 2026. CC BY 4.0 License.

3 Results

3.1 Hydrographic and circulation structure

3.1.1 Surface circulation

On 6 December 2023, sea-surface height (Fig. 1a) showed a central depression, with surface currents organised counter-clockwise, indicating a basin-scale cyclonic gyre at the entrance of the Gulf of Taranto. This pattern coincided with strong wind stress over the Gulf (see below).

The 2023 monthly cycle of area-averaged wind-stress (Fig.S1b) indicated strong late-autumn wind forcing with wind stress exceeding 0.14 N m^{-2} (Fig. S1a, b) and wind stress curl, computed from the same product, exceeding 1.05×10^{-5} N m^{-3}, consistent with positive curl and Ekman pumping over the Gulf. Together, the SSH pattern and the intense winds are consistent with surface divergence and a lowering of sea level at the gyre centre. The cyclonic state sampled here is one phase of the basin-scale variability described for this region (Borzelli et al., 2009; Civitarese et al., 2010; Federico et al., 2020). That variability is quasi-decadal and can reverse the gyre entirely: the Gulf was anticyclonic in 2014 and cyclonic in 2016, and cyclonic states dominate the 1993–2018 altimetric record with intermittent anticyclonic episodes (Federico et al., 2020). A single snapshot cannot assign it to a phase of the Adriatic-Ionian Bimodal Oscillating System, nor separate a BiOS-related circulation state from mesoscale displacement of the gyre.

This surface structure is coherent with the doming of isopycnals and uplift of subsurface layers observed in the vertical sections described below. At the surface, the fresher layer visible in the salinity and velocity sections is consistent with the advection of low-salinity Adriatic-derived water entering along the eastern side of the section, associated with the Western Adriatic Coastal Current (WACC) system (Artegiani et al., 1997a, b; Guarnieri et al., 2013; Federico et al., 2017). This inflow is compensated by a return flow on the western (opposite) side of the section, directed out of the Gulf, yielding the cross-Gulf overturning expected under cyclonic conditions. The resulting divergence enhances the upward displacement of density surfaces and favours the vertical transfer of tracers into the upper and intermediate layers.

3.1.2 Velocity field

The cross-section velocity field (Fig. 1b), obtained by projecting the LADCP profiles onto the section heading rather than from a geostrophic calculation, reveals a strong structured circulation composed of alternating inflow and outflow veins from the surface to the deep layers. In the upper layer, an Adriatic inflow enters from the eastern slope with velocities starting from 0.15 m s^{-1}, and a flow of similar intensity emerges from the western side of the gulf, suggesting a recirculation of this surface stream within the gulf (also highlighted by the circulation structure shown in Fig. 1a). Subsurface structures are complex: on the eastern slope, an outflow occurs at ~300 m, a strong inflow near 1300 m ($\sigma_\theta \approx 29.19$ kg m^{-3}), and another inflow between 2000–2300 m. No coherent eastern inflow of intermediate water is resolved in the velocity section, and EIW-core is a net export across the transect (−0.30 ± 0.24 Sv, Fig. 4i) consistent with the absence of an intermediate inflow signature in Fig.1b.

https://doi.org/10.5194/egusphere-2026-6912
Preprint. Discussion started: 12 November 2026
© Author(s) 2026. CC BY 4.0 License.

On the western slope, localized inflows are observed near 300 m and 1000 m within a water column dominated by outflow, while a strong outflow is centred at ~1500–1700 m (σ_θ> 29.2 kg m^{-3}). The western side of the section is dominated by outflow in the upper 0–500 m. These alternating jets define marked vertical and lateral shear zones across the section.

3.1.3 Thermohaline structure

CT (isotherms) and SA field (colour shading), both shown in Fig. 1c, display pronounced east-west gradients. Between about 70 and 300 m the isopycnals dome upward in the centre of the section, lifting relatively cool water into the subsurface. This water is fresher than the intermediate layer beneath it, though not fresher than the surface layer above. On the flanks, and most clearly to the east, the intermediate salinity maximum associated with EIW-core (SA ≈ 39.18- 39.20) rises toward the edges of the dome. This vertical layering emphasizes the interplay of fresher surface waters and saltier intermediate waters of eastern origin across the section. The spiciness section (Fig. S1c) supports this interpretation by showing a low-spiciness core co-located with the uplifted isopycnals in the centre of the transect. In contrast, the flanks of the dome, especially on the eastern side, are characterized by higher spiciness values consistent with saltier intermediate waters. The resulting along-isopycnal spiciness gradients indicate strong lateral contrasts in water-mass properties around the cyclonic dome.

https://doi.org/10.5194/egusphere-2026-6912
Preprint. Discussion started: 12 November 2026
© Author(s) 2026. CC BY 4.0 License.

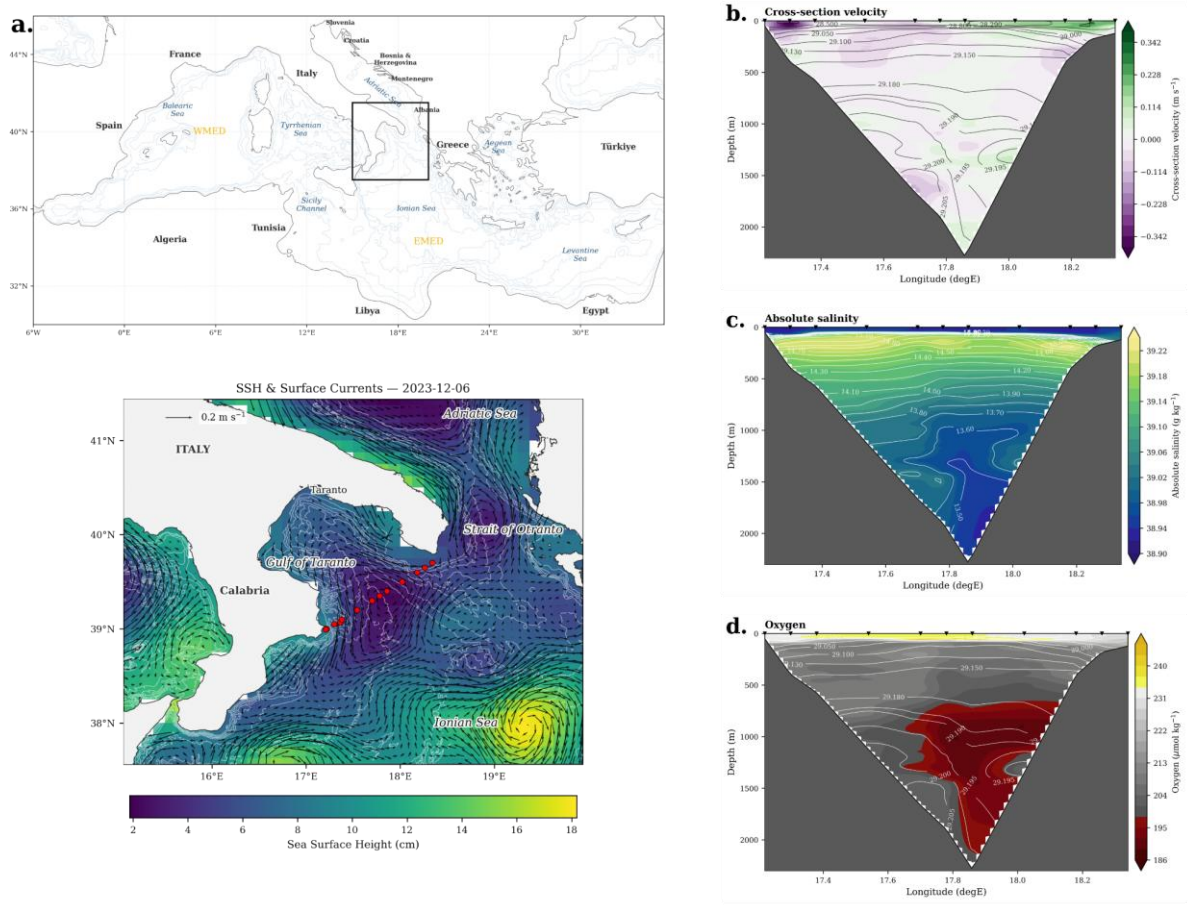


Figure 1: Hydrographic and circulation structure at the entrance of the Gulf of Taranto during the PIONEER-2023 cruise. (a) bathymetry and CTD/LADCP stations with sea-surface height field (colour scale) and surface geostrophic currents (arrows; reference vector shown over land) for 6 December 2023.(b) Cross-section velocity (m s⁻¹);with green indicates inflow and violet indicates outflow, with grey potential-density contours (σ_0, kg m⁻³). (c) Vertical section of Absolute Salinity (SA, g kg⁻¹) with superimposed Conservative Temperature isotherms (CT, °C). (d) Vertical section of dissolved oxygen (DO, µmol kg⁻¹) with overlaid potential-density contours (σ_0), highlighting the OML.

3.2 Biogeochemical features and tracer distributions

3.2.1 Dissolved inorganic nutrients

The vertical distributions of nitrate, phosphate, and silicic acid reveal a strong imprint of the hydrographic structure and cyclonic circulation at the entrance of the Gulf of Taranto (Fig. 2a, b, c). All nutrients are strongly depleted in the near-surface layer, with concentrations of nitrate below 0.5 μmol kg^{-1}, of phosphate below 0.2 μmol kg^{-1}, and of silicic acid below 1.2 μmol kg^{-1}. Beneath the surface, however, the three nutrients show distinct vertical and lateral structures, indicating that their distributions are controlled by stratification, water-mass advection, isopycnal uplift, and interior remineralization of organic

https://doi.org/10.5194/egusphere-2026-6912
Preprint. Discussion started: 12 November 2026
© Author(s) 2026. CC BY 4.0 License.

matter. The imprint of the cyclonic circulation is particularly evident between about 17.6°E and 18.0°E, where domed isopycnals are accompanied by upward displaced nutrient isolines. At the transect edges, around 17.2-17.4°E and 18.1-18.3°E, the same isoline is displaced downward. This contrast shows that nutrient-rich waters are uplifted beneath the cyclonic dome, bringing the nutracline closer to the surface in the central part of the transect.

Nitrate concentrations are lowest in the upper layer and increase below the mixed layer, but the vertical section does not show a simple monotonic increase toward the bottom. Instead, there is a broad subsurface to intermediate enrichment, with a pronounced maximum centred near 17.7-17.8°E at about 900-1200 m. This maximum lies close to the density interval associated with the OML. Below the mid-depth maximum, nitrate concentrations decrease slightly but remain relatively high in the deep layer.

Phosphate distribution exhibits a more spatially confined subsurface maximum than nitrate. Surface concentrations are low, while a pronounced maximum develops in the central part of the transect, centred near 17.75-17.85°E and roughly at 1100-1400 m depth. This maximum coincides with the depth range of lowest oxygen. Outside this central maximum, phosphate concentrations remain elevated on the eastern side of the deep layer, whereas lower values persist on the western side.

Silicic acid distribution exhibits the strongest vertical increase among the three nutrients and the clearest deep enrichment. Concentrations remain low near the surface, increase progressively through the intermediate layers, and reach their highest values in the central-eastern deep layer between about 1200 and 1700 m depth, with a maximum near 17.8-17.9°E. Compared to nitrate and phosphate, silicic acid shows a stronger accumulation in the deeper layer, and retains a marked lateral structure, indicating that deep exchange and intrusive veins modulate its distribution.

Localized deep anomalies further intersperse the section. In the central-eastern deep layer, nutrient enrichment coincides with the density range associated with the OML and with weakly ventilated waters occupying the sill region. On the western side, nutrient concentrations are generally lower in the layer associated with the oxygen-rich western slope feature. These lateral contrasts suggest strong tracer gradients over relatively short horizontal scales. A longitudinal gradient is also evident in phosphate, with generally higher values on the eastern side. This enrichment is consistent with lateral contrasts in water mass properties along the eastern side of the transect, although the sampled transect alone does not allow the relative influence of WACC-related inputs and coastal contributions to be separated explicitly.

Overall, nutrient vertical sections show that nitrate, phosphate and silicic acid are structured by a combination of upper layer depletion, cyclonic uplift, lateral water mass contrast, and intermediate to deep layers accumulation with the OML and adjacent deep waters.

3.2.2 Dissolved inorganic carbon and total alkalinity

DIC and TA show a clear relationship with the hydrographic structure at the entrance of the Gulf of Taranto (Fig. 2d, e), but they emphasize partly different aspects of the carbonate system. DIC displays its lowest concentrations in the near-surface layer and increases sharply below the mixed layer, forming a broad subsurface to intermediate enrichment. This enriched layer

https://doi.org/10.5194/egusphere-2026-6912
Preprint. Discussion started: 12 November 2026
© Author(s) 2026. CC BY 4.0 License.

is uplifted in the centre of the transect together with the domed isopycnals, most clearly between about 17.7°E and 18.0°E, indicating that cyclonic uplift brings DIC-enriched subsurface waters toward shallower layers. The DIC maximum is not located in the deepest part of the transect, but mainly within the subsurface and intermediate layers. Below about 1000 m, DIC shows weaker vertical gradients, suggesting a more homogeneous deep carbonate reservoir with localized lateral anomalies that coincide with the deep circulation structure: slightly higher DIC in the eastern deep inflow (EMDW-ad) and lower values in the western deep outflow. These anomalies reflect differences in water-mass history and ventilation rather than a simple monotonic increase of DIC with depth.

This vertical structure is confirmed and clarified by the property–property relationships computed on the discrete samples and colour-coded by water-mass class (Fig. S2). In the DIC–AOU plane (Fig. S2b), DIC increases with apparent oxygen utilization (AOU) along the ventilated upper layers, reaching a maximum near AOU ≈ 26 µmol kg^{-1}, (slope 1.40, 95 % confidence interval (CI): 0.64–2.16; R^2 = 0.62, n = 12; Fig. S2b). The confidence interval spans both reference stoichiometries, so the upper-water fit is consistent with aerobic remineralization but does not constrain the ratio. Beyond this point, DIC decreases monotonically as AOU increases across EIW-down → EMDW-ad → EMDW-r → OML. Consequently, the deep classes fall progressively below both the observed positive relationship in the ventilated upper layers and the reference remineralization slopes of Redfield et al. (1963) and Anderson and Sarmiento (1994). Of the two deep water classes, EMDW-r is more oxygen-depleted than EMDW-ad (AOU 52.9 against 46.2 µmol kg^{-1}) but has a lower DIC concentration (≈2321 versus ≈2331 µmol kg^{-1}). The three samples classified as OML have even lower DIC concentrations. This pattern contrasts with the more familiar situation in which the older, more oxygen-depleted waters contain more DIC. The decoupling indicates that interior DIC here is governed by water-mass provenance and preformed properties rather than by in-situ respiration: total DIC is the sum of a preformed component and a respiratory term (≈ C:O_2 × AOU), and the deep classes combine a low preformed DIC with an AOU that is not a clean respiration proxy. The deep classes are therefore not anomalous: their low DIC at high AOU is consistent with formation under a lower atmospheric CO_2 than that of the overlying waters, an argument developed in Sect. S1 of the Supplement. This is mirrored in pH (Fig. S2c), which declines from the surface to a minimum in EIW-core near AOU ≈ 28 µmol kg^{-1} and then increases again through EIW-down, EMDW-ad and EMDW-r toward the highest AOU values. The reversal of both DIC and pH beyond intermediate AOU is the signature expected if interior carbonate chemistry is set by provenance rather than by progressive respiration.

TA shows a partly similar vertical structure, but its distribution is organised by water mass rather than by salinity. A class-based comparison (Fig. S2a) shows that TA is essentially uniform across the surface and intermediate classes (≈2632–2635 µmol kg^{-1}) despite a salinity range of more than 0.2 g kg^{-1}, and is systematically lower in the deep classes (EMDW-ad ≈2627, EMDW-r ≈2623, OML ≈2618 µmol kg^{-1}) at salinities that overlap those of the surface layer. The two surface branches are not distinguishable from one another (≈2635 ± 2 and ≈2632 ± 2 µmol kg^{-1} for the western and eastern branches), so the section-scale TA field does not by itself isolate an Adriatic-influenced surface end-member.

https://doi.org/10.5194/egusphere-2026-6912
Preprint. Discussion started: 12 November 2026
© Author(s) 2026. CC BY 4.0 License.

Consistent with this pattern, TA shows no systematic relationship with salinity across the section: the local TA–SA regression is flat and non-significant (slope 4.0 ± 16.6 µmol kg^{-1} per g kg^{-1}, R^2 = 0.002, p = 0.63, n = 98; Fig. S2a). In the open Mediterranean TA and salinity are usually strongly and positively correlated, because evaporation concentrates alkalinity together with salt (Copin-Montégut, 1993; Schneider et al., 2007; Álvarez et al., 2014), whereas in the Adriatic high-alkalinity riverine inputs raise TA in low-salinity waters and produce an inverse relationship (Cantoni et al., 2012; Ingrosso et al., 2016; Cantoni et al., 2024). At the entrance of the Gulf of Taranto, neither relationship is observed because the low-salinity end of the section is represented by both the highest-alkalinity (surface) and the lowest-alkalinity (deep) waters sampled. The absence of a section-wide TA–SA slope therefore reflects the vertical distribution of alkalinity among the different water mass; it cannot be used to identify end-members, and it does not exclude localized coastal alkalinity inputs. TA is most useful here as a marker of the depth-ordered provenance of the classes rather than as a salinity-based mixing tracer.

In the upper and intermediate layers, TA also exhibits an east-west contrast, with higher values associated with the eastern and intermediate classes, and a subsurface TA maximum consistent with the influence of saltier EIW and its mixing with surrounding waters. Below roughly 600–800 m, this intermediate signature weakens and TA becomes more homogeneous, varying only weakly at depth apart from localized anomalies associated with the deep inflow-outflow structure (slightly higher near the eastern deep inflow, lower within the western deep outflow). Overall, DIC and TA are partly coupled through water-mass structure and mixing, yet they carry distinct information and permit different interpretations. DIC mainly integrates the effect of physical uplift, preformed properties, water-mass age, and remineralized carbon. its deviation from Redfield-based expectations at depth (Fig. S2b) indicates that the deep carbonate distribution is controlled primarily by water-mass provenance and ventilation history rather than by local respiration. TA, in turn, primarily reflects source-water differences, particularly the contrasting TA–SA signature of the Adriatic end-member, characterized by an inverse relationship, and the open-Mediterranean end-member, characterized by a positive relationship. Consistent with this, the strongest carbonate anomaly occurs at intermediate rather than maximum AOU, showing that no single depth- or oxygen-dependent regeneration pathway can explain the carbonate system across all water-mass classes.

3.2.3 Dissolved oxygen and apparent oxygen utilization

Dissolved oxygen (DO, Fig. 1d) shows a distinct OML centred in the mid-eastern Gulf at ~1000 m. The OML is the least ventilated part: its class-mean oxygen (190.2 μmol kg^{-1}, Table 1) is the lowest of all classes, below both the resident EMDW-r (195.2 μmol kg^{-1}) and the Adriatic-derived EMDW-ad (200.6 μmol kg^{-1}). The lower part of the OML lies close to the density range where the EMDW-ad intrusions are observed, while its upper boundary is associated with double-diffusive instability regimes, as indicated by Turner angle/density-ratio conditions favourable to staircase-like structure.

Below the OML, relatively oxygen-rich veins that are also saltier than the OML core are observed. An inflow from the east occurs at ~1390 m, near $\sigma_\theta \approx 29.195$ kg m^{-3}, while a westward outflow is centred at ~1590–1650 m at $\sigma_\theta > 29.2$ kg m^{-3}. These veins are characterized by relatively high temperature and salinity, with DO concentrations reaching ~205 μmol kg^{-1}.

https://doi.org/10.5194/egusphere-2026-6912
Preprint. Discussion started: 12 November 2026
© Author(s) 2026. CC BY 4.0 License.

By contrast, the resident deep-water core on the eastern side of the section, below ~1000 m is colder, fresher, and represents the least ventilated part of the deep layer, with DO < 197 µmol kg⁻¹, consistent with the resident weakly ventilated EMDW, although the section-wide oxygen minimum occurs in the overlying OML.

On the western side, oxygenated layers extend deeper, and a local DO maximum of ~205 μmol kg⁻¹ occurs near 600 m, showing that the OML is not laterally uniform across the transect.

AOU (Fig.2f) varies systematically with depth and water mass. Near the surface, AOU ranges from approximately −4 to 0 μmol kg^{-1}, indicating DO saturation or weak supersaturation in the upper layer. AOU then increases progressively with depth, and reaching a section maximum of 58.9 µmol kg⁻¹ within the OML ($\sigma_0 \approx 29.184–29.195$ kg m⁻³). At this location, near 1010 m at 17.80°E, DO reaches its section minimum of 188.8 µmol kg⁻¹. This maximum is centred in the central-eastern part of the transect, between about 17.7°E and 18.0°E and 700-1200 m where DO is lowest. The AOU section also shows marked lateral heterogeneity below about 500 m. On the western side of the transect, around 17.4°E -17.6°E, AOU values near 600 m are lower than in the central-eastern side at the same depth. This pattern is corresponding to the local DO maximum identified in the oxygen vertical section. Below the OML, AOU decreases again within the depth range of the deeper oxygenated veins, between 1300 and 1600 m. The spatial coherence between AOU and the other tracers is most evident within the OML depth range. Where AOU is highest, and DO reaches its minimum, phosphate and silicic acid are elevated, and spiciness is reduced. However, DIC and TA are relatively lower within this same layer than in some adjacent intermediate waters, indicating that the carbonate-system tracers are not organised identically to AOU and nutrients.

Overall, the DO and AOU vertical sections identify the central-eastern OML as the main oxygen-consumption maximum along the transect and highlights strong lateral contrasts in ventilation state, particularly between the OML core, the western mid-depth oxygen feature, and the deeper oxygenated veins.

https://doi.org/10.5194/egusphere-2026-6912
Preprint. Discussion started: 12 November 2026
© Author(s) 2026. CC BY 4.0 License.

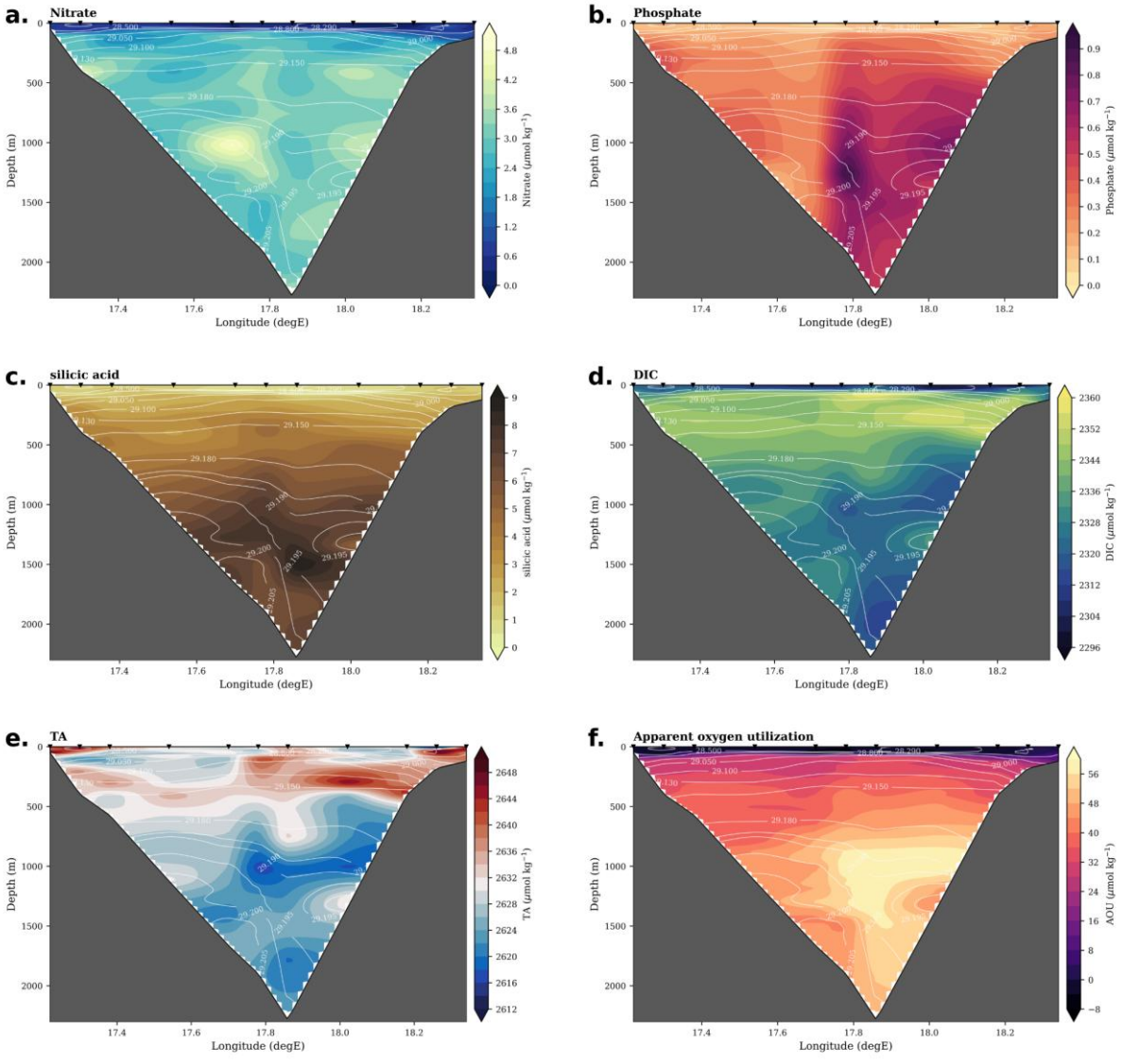


Figure 2: Biogeochemical sections across the Gulf entrance. Vertical sections show (a) nitrate (µmol kg⁻¹), (b) phosphate (µmol kg⁻¹), (c) silicic acid (µmol kg⁻¹), (d) dissolved inorganic carbon (DIC, µmol kg⁻¹), (e) total alkalinity (TA, µmol kg⁻¹), and (f) apparent oxygen utilization (AOU, µmol kg⁻¹). White contours show σ_0 (kg m⁻³). Bottle-derived fields are objectively mapped.

3.3 Water masses, binning, and interfaces of interest

To interpret the circulation in terms of dynamically and biogeochemically distinct layers, we identify the principal water masses along the transect using the combined thermohaline, oxygen, spiciness and geographical structure (Fig. 3). The resulting classes are ISW/AW-w, ISW/AW-e, EIW-core, EIW-down, OML, EMDW-ad, and EMDW-r. These classes

https://doi.org/10.5194/egusphere-2026-6912
Preprint. Discussion started: 12 November 2026
© Author(s) 2026. CC BY 4.0 License.

represent mixed hydrographic-biogeochemical regimes rather than unmixed source water masses. They provide the framework for calculating cross-sectional transport budgets and vertical diffusive fluxes across density defined interfaces of interest (IOIs). The terminology follows Budillon et al. (2010), with local subclasses retained to represent the lateral structure of the section.

The CT-SA diagram (Fig. 3a) shows the expected stratification of the Gulf of Taranto. The upper layer consists of relatively fresh and warm Ionian/Atlantic-derived surface water of Adriatic influence. It is divided geographically into western (ISW/AW-w) and eastern (ISW/AW-e) branches. Beneath this layer, EIW-core represents the mixed LIW/CIW layer associated with the salinity maximum, occupying a narrow range of SA = 39.15-39.17 and CT = 14.9 -15.2°C. EIW-down forms the transition toward the colder and slightly fresher deep waters and constitutes the thickest individual class, occupying close to two-fifths of the sampled water column. At greater depths, the OML, EMDW-ad, and EMDW-r occupy partially overlapping thermohaline and density ranges. Their separation required the combined use of DO, spiciness, and position within the section. The oxygen-density relationship (Fig. 3b) complements the CT-SA structure: surface waters are the most oxygenated, EIW-core occupies an intermediate oxygen range and the oxygen minimum defining the OML occurs σ_0 = 29.184 and 29.195 kg m^{-3}. this density interval is used below to define its bounding interfaces.

The spatial distribution of the classes is shown in Fig. 3c. The surface branches occupy different lateral portions of the upper section, while the EIW-core forms a relatively continuous intermediate cap above the thicker EIW-down layer. The OML forms a distinct central to central-eastern lens. Beneath and around it, EMDW-r forms an enclosed resident core concentrated on the central-eastern side of the section, extending from approximately 1000 m to the deepest sampled levels near 2270 m. EMDW-ad forms a shallower envelope, mainly between roughly 700 and 1800 m, wrapping around the resident core. It occurs predominantly on the western flank and reappears in the eastern flank, where it enters the section. Density alone cannot separate the two deep classes. EMDW-r lies entirely within the density range of EMDW-ad: σ_0 = 29.193 to 29.207 for EMDW-r and 29.186 to 29.207 kg m^{-3} for EMDW-ad. Their median densities differ by only 0.0005 kg m^{-3} (29.1966 and 29.1971 kg m^{-3}, respectively), and both reach the same maximum density of 29.209 kg m^{-3}. Their classification therefore rests primarily on their geometry and relative ventilation states. EMDW-ad is laterally confined, entering on the eastern side, where 80 % of its grid points are associated with inflow, and leaving on the western side. The median depth of its inflowing and outflowing cells is approximately 1230 and 1020 m, respectively. These values are class medians over the full lateral extent of the vein and are shallower than the velocity cores of the deep jets reported under Velocity field. Consistent with this geometry, EMDW-ad is better ventilated than EMDW-r, with mean DO concentrations of 200.6 and 195.2 µmol kg^{-1} and AOU values of 46.2 and 52.9 µmol kg^{-1}, respectively. Its section-integrated transport is indistinguishable from zero for all tracers, consistent with the near-cancellation of eastern inflow and western outflow. Nutrient concentrations differ in the same direction (phosphate are 0.39 and 0.61 µmol kg^{-1} and silicic acid are 6.2 and 7.2 µmol kg^{-1}) in the EMDW-ad and EMDW-r, respectively. However, fewer than 20 discrete bottle samples were collected below 1000 m. Deep nutrient transports and fluxes across the deepest interface must therefore be interpreted cautiously and are not used as independent evidence for assigning the deep classes.

https://doi.org/10.5194/egusphere-2026-6912
Preprint. Discussion started: 12 November 2026
© Author(s) 2026. CC BY 4.0 License.

EMDW-ad is warmer and saltier than EMDW-r (13.74 °C and 39.03 g kg^{-1} against 13.51 °C and 38.96 g kg^{-1}), the opposite of the classical picture in which Adriatic dense water is the colder, fresher end-member of EMDW. This is consistent with the two classes having formed at different times against a warming, salinization Adriatic background rather than with a difference in provenance (see Sect. S1 of the Supplement). Terzić et al. (2025) also reported a reversal of the deep Adriatic density trend after 2006, with density decreasing by approximately 0.03 µmol kg^{-1} per decade because warming outpaced salinization. The trend is consistent with the absence of a resolvable density difference between EMDW-ad and EMDW-r: recently formed Adriatic water is no longer necessarily the densest end-member. The relatively low DIC of EMDW-r despite its high AOU (see Dissolved inorganic carbon and total alkalinity) is also consistent with difference in formation-period. However, these thermohaline and biogeochemical contrasts support, but do not independently establish, the geometrical classification, since mixing with overlying water can displace deep-water properties in the same direction as a younger source. accordingly, ventilation is used here in a relative sense: EMDW-ad is better ventilated than EMDW-r, but is not necessarily recently ventilated in absolute terms. Table 1 summarizes the fraction, mean properties, and regional interpretation of each class. Based on this classification, four density-centred IOIs are defined to quantify vertical diffusive fluxes across the principal water-mass boundaries:

(i) σ_o = 29.120 kg m^{-3}, the interface between EIW-core and EIW-down;

(ii) σ_0 = 29.184 kg m^{-3}, defining the upper boundary of the OML, between EIW-down and the OML.

(iii) σ_0 = 29.195 kg m^{-3}, defining the lower boundary of the OML, and its diffusive contact with EMDW-r; and

(iv) σ_0 = 29.203 kg m^{-3}, lying within the EMDW domain and quantifying diapycnal exchange within the deep layer rather than between EMDW-r and EMDW-ad, which share the same density range and are in lateral rather than density contact.

Defining these interfaces in density rather than depth coordinates follows the natural stratification of the water column and captures the pathways along which turbulent exchange, tracer transfer, and water-mass transformation occur. The section-integrated exchange Associated with these classes is presented under Tracer transports across the section.

https://doi.org/10.5194/egusphere-2026-6912
Preprint. Discussion started: 12 November 2026
© Author(s) 2026. CC BY 4.0 License.

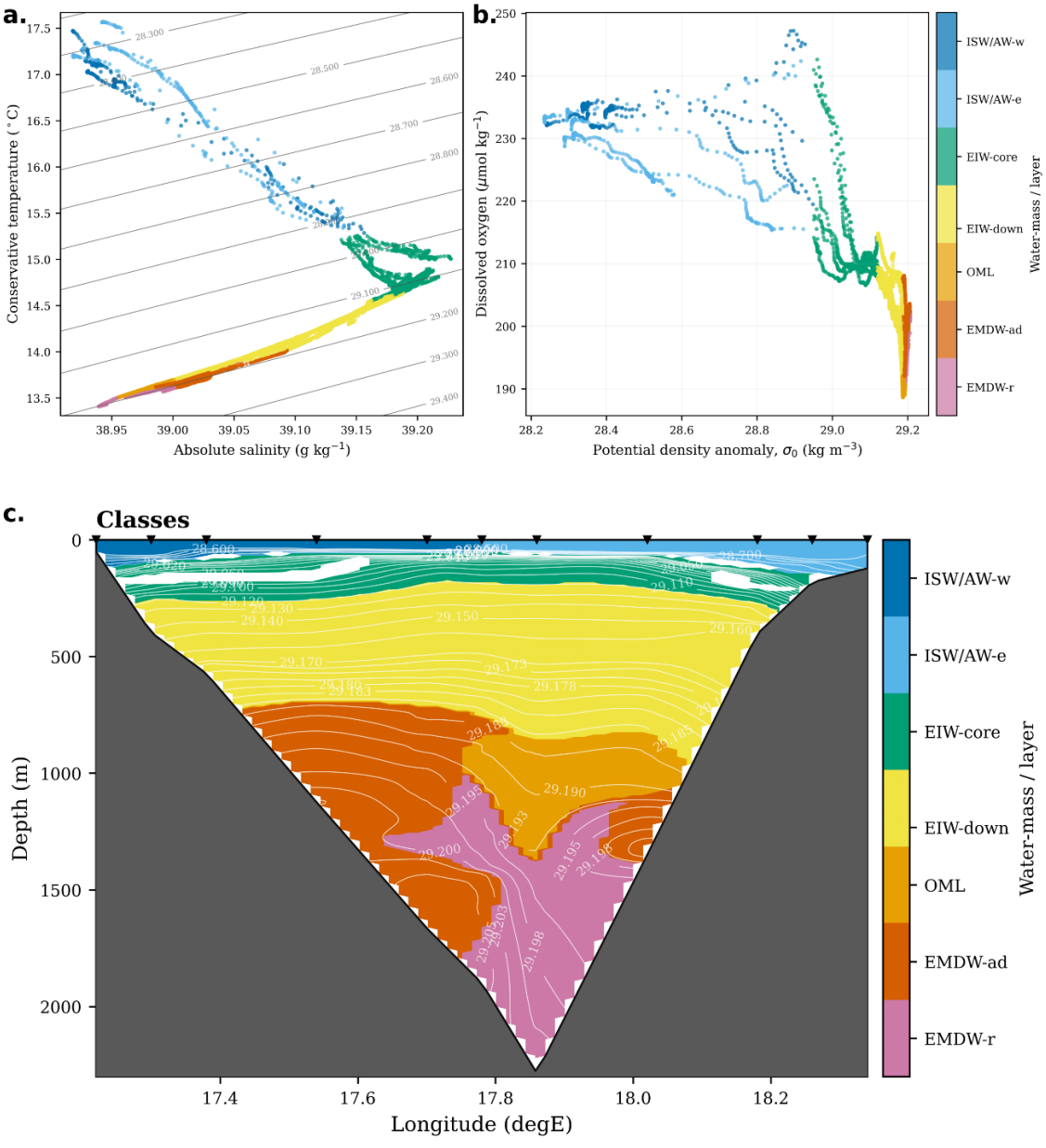


Figure 3: Hydrographic-biogeochemical classification. (a) CT-SA diagram with σ₀ contours; colours denote the seven local classes. (b) Dissolved oxygen as a function of σ₀ for the same classes. (c) Section distribution of the classes with σ₀ contours. The labels identify mixed regimes and transport branches, not necessarily pure source-water masses.

https://doi.org/10.5194/egusphere-2026-6912
Preprint. Discussion started: 12 November 2026
© Author(s) 2026. CC BY 4.0 License.

Table 1: Hydrographic-biogeochemical classes along the transect. N is the number of classified cells on the 1 m CTD profile grid; Fraction is the percentage of all classified cells; CT, SA, π, and O_2 are class means.

Layer	label	Bin ID	(N)	Fraction (%)	Mean CT (°C)	Mean SA (g kg^{-1})	Mean π	Mean O_2 (μmol kg^{-1})
Surface	ISW/AW-w	1	290	3.48	16.66	38.98	5.513	232.96
	ISW/AW-e	2	377	4.53	16.85	38.98	5.557	229.96
Intermediate	EIW-core	3	997	11.98	14.84	39.18	5.219	211.29
	EIW-down	4	3156	37.91	14.18	39.11	5.007	204.16
Transitional	OML	5	701	8.48	13.6	38.98	4.78	190.15
Deep	EMDW-ad	6	1538	18.48	13.74	39.028	4.84	200.6
	EMDW-r	7	1265	15.20	13.5	38.963	4.74	195.24

3.4 Tracer transports across the section

The water mass transport budgets show that the exchange across the entrance of the Gulf of Taranto is organised by an asymmetric cyclonic circulation (Fig. 4). With our sign convention, positive transport denotes inflow and negative transport denotes outflow toward the open Ionian Sea. Figure 4a illustrates the general inflow/outflow structure during the survey: EMDW-ad enters on the central-eastern side of the transect and exits on the western side, while the EMDW-r shows a net inflow. EMDW-r contribution is consistently positive across all tracers although its magnitude is only 1.4-1.8 times the estimated uncertainty, u. By contrast, the section-integrated EMDW-ad flux is indistinguishable from zero for every tracer ($|flux|/u \leq 0.5$), consistent with a thorough flowing vein whose eastern inflow and western outflow largely cancel the section integrated budget. The OML contribution is negligeable. In the upper layer the cumulative transport highlights the cyclonic structure, although the gyre is not perfectly centred: eastern surface-water inflow (ISW/AW-e) enters near 18.3°E, balanced by outflow near 17.7°E, with an additional outflow further west near 17.3°E. This asymmetry reflects the lateral displacement of the cyclonic gyre and frames the tracer budgets.

Before interpreting each individual branch, we stress that the section-integrated (net) transport is not statistically distinguishable from zero for any tracer: the net term ("ALL" in Fig. 4b–h) is several times smaller than its combined propagated and bootstrap uncertainty (net salt $-6.7\times10^{9} \pm 4.0\times10^{10}$ g s^{-1}; net oxygen $-3.0\times10^{10} \pm 2.2\times10^{11}$; net DIC $-4.1\times10^{11} \pm 2.4\times10^{12}$; net TA $-4.4\times10^{11} \pm 2.7\times10^{12}$; net nitrate $-1.5\times10^{9} \pm 2.5\times10^{9}$; net phosphate $+7.3\times10^{7} \pm 3.3\times10^{8}$; net silicic acid $-8.9\times10^{8} \pm 4.7\times10^{9}$ μmol s^{-1}). The net is weakly negative for most tracers and weakly positive for phosphate, but in every case $|net|/u \leq 0.6$. A positive net would imply net import and, in the absence of compensating sinks, accumulation within the Gulf; a negative net would imply the reverse. Because none of the net transport is significant, we do not interpret the section as a net source or sink for any tracer. The robust result is instead the branch-level compensation described below, which is significant even where the net transport is not. Among the branches, the eastern surface inflow (ISW/AW-e) is the only robust term,

https://doi.org/10.5194/egusphere-2026-6912
Preprint. Discussion started: 12 November 2026
© Author(s) 2026. CC BY 4.0 License.

exceeding its uncertainty by a factor of ~3–5 for every tracer (e.g., salt $+3.4\times10^{10} \pm 7.2\times10^{9}$ g s^{-1}, 4.7u; oxygen $+2.0\times10^{11} \pm 4.2\times10^{10}$, 4.8u; DIC $+2.0\times10^{12} \pm 4.3\times10^{11}$, 4.7u).

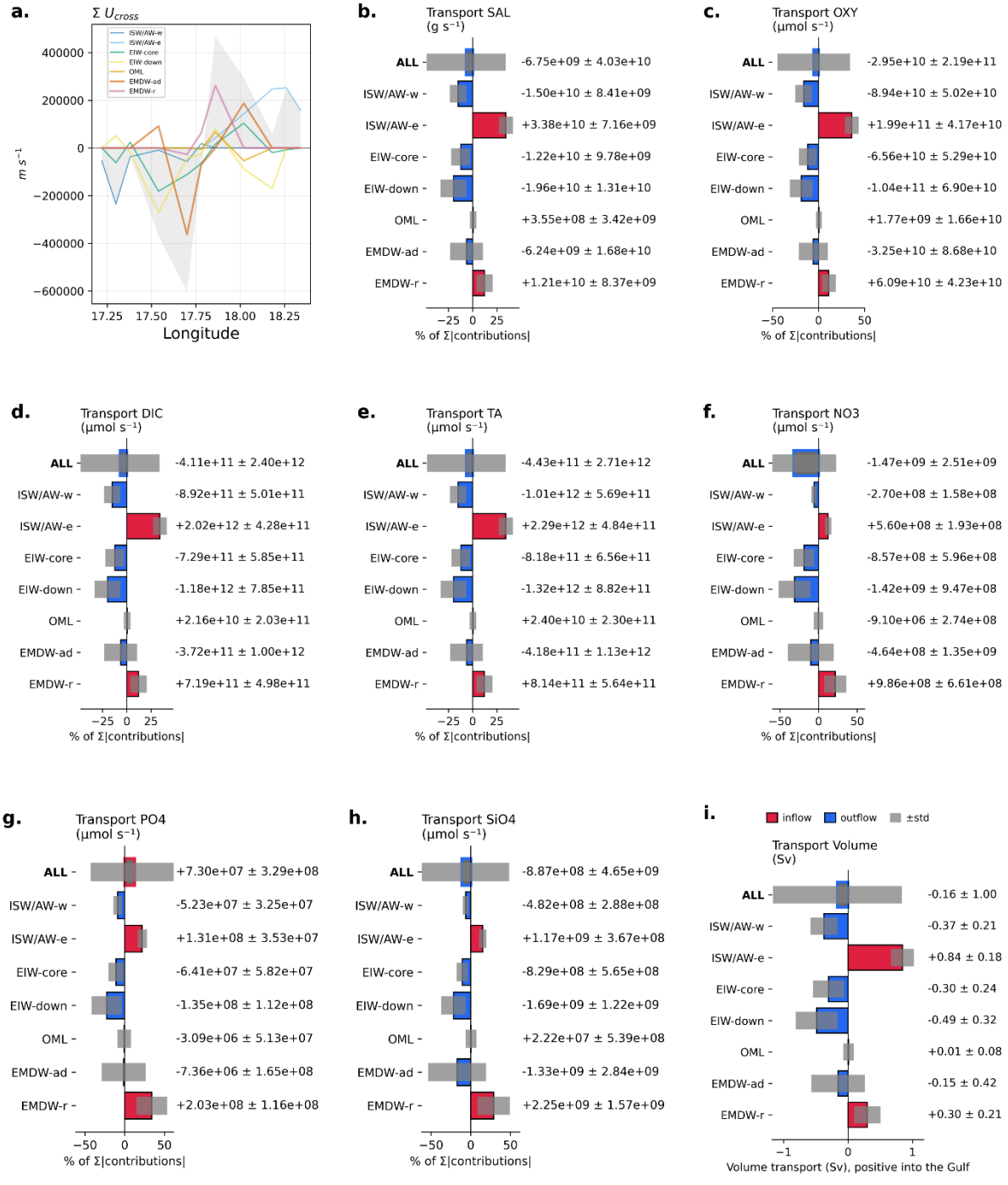
The deep class (EMDW-r) is the second inflowing branch, consistently positive across tracers but only marginally significant (e.g., phosphate $+2.03\times10^{8} \pm 1.2\times10^{8}$, 1.8u). These inflows are compensated by exports in the western surface branch (ISW/AW-w) and the intermediate and transitional classes (EIW-core, EIW-down), each marginal (~1–2u). Salinity and oxygen, the tracers least affected by internal sources and sinks, show this geometry most clearly. Salt is imported by ISW/AW-e (robust) and EMDW-r (marginal) and exported by ISW/AW-w, EIW-core and EIW-down. Oxygen has the same structure with an even stronger deep signal: ISW/AW-e and EMDW-r import oxygen while ISW/AW-w, EIW-core and EIW-down export it, indicating that interior renewal is linked primarily to the robust eastern surface inflow and, secondarily, to the marginal deep intrusion.

DIC and TA broadly follow the same inflow-outflow geometry, with the largest inflow carried by ISW/AW-e and a secondary, marginal contribution from EMDW-r, opposed by export in ISW/AW-w, EIW-core and EIW-down. We note that DIC is not a conservative tracer (it is modified by remineralization and air-sea exchange, and oxygen likewise is non-conservative); the fact that its section transport nonetheless follows the water-mass geometry indicates that advection dominates the DIC and TA budgets during the survey. Because DIC and TA nets are within uncertainty, we do not conclude that the Gulf is a net carbon or alkalinity sink; a detailed source/sink assessment would additionally require the air-sea and biological terms.

Nutrient budgets carry a stronger deep-water imprint than salinity and oxygen. For nitrate, the largest inflow is the deep branch (EMDW-r, $+9.9\times10^{8} \pm 6.6\times10^{8}$, 1.5u), with a smaller but robust inflow from ISW/AW-e ($+5.6\times10^{8} \pm 1.9\times10^{8}$, 2.9u), opposed by export in EIW-down (largest), EIW-core and ISW/AW-w; the OML is negligible or within uncertainty. Silicic acid is the most deep-branch-dominated nutrient: its largest inflow is carried by EMDW-r ($+2.3\times10^{9} \pm 1.6\times10^{9}$) and a robust secondary inflow by ISW/AW-e ($+1.2\times10^{9} \pm 3.7\times10^{8}$), while EIW-down exports it and the EMDW-ad contribution are not resolved consistent with the strong deep silicic acid enrichment seen in the vertical section. Phosphate is likewise deep-inflow dominated (EMDW-r largest and marginally significant at 1.8u, ISW/AW-e robust at 3.7u), with export by EIW-down, EIW-core and ISW/AW-w; the OML and EMDW-ad contributions are not significant, so we do not attribute phosphate import to intermediate regeneration. Overall, the transports describe an asymmetric but compensated exchange structure: robust inflow through the eastern surface branch (ISW/AW-e), a marginal deep inflow (EMDW-r), and an Adriatic-derived vein (EMDW-ad) that circulates through the section without a resolvable net contribution, balanced by marginal export through the western surface branch and the intermediate and transitional waters. Because the section-integrated residuals are within uncertainty, the robust signal is this water-mass partitioning of the exchange rather than any net section-scale source or sink. Inflow totals +1.15 Sv (Fig. 4i) (ISW/AW-e +0.84±0.18 Sv; EMDW-r +0.30±0.21 Sv; OML +0.01±0.08 Sv) and outflow -1.31 Sv (EIW-down -0.49 ±0.32 Sv; ISW/AW-w -0.37±0.21 Sv; EIW-core -0.30±0.24 Sv; EMDW-ad -0.15±0.42 Sv, the last of which is not resolved

https://doi.org/10.5194/egusphere-2026-6912
Preprint. Discussion started: 12 November 2026
© Author(s) 2026. CC BY 4.0 License.

(0.4u) and is listed with the outflow branches only for completeness), leaving a net of -0.16 ±1.00 Sv that is indistinguishable from zero. The eastern surface inflow is the only class resolved at better than four standard errors.



https://doi.org/10.5194/egusphere-2026-6912
Preprint. Discussion started: 12 November 2026
© Author(s) 2026. CC BY 4.0 License.

Figure 4: Water-mass-resolved volume and tracer transports the transect. (a) Cross-transect velocity integrated within each water-mass class and displayed as longitudinal intervals. Coloured bars indicate contribution of individual water-mass classes; grey shaded bands show the cumulative transport obtained by summing all classes. (b)-(h) Integrated transports of (b) salinity, (c) dissolved oxygen, (d) DIC,(e) total alkalinity, (f) nitrate, (g) phosphate, (h) silicic acid, separated by water-mass class. Bars are normalized to the percentage of the absolute total contribution for each tracer; horizontal scale is specific to each panel; red indicates inflow and blue indicates outflow. Class transports are reported on the right in the units given in each panel title, with the net total (ALL) shown at the top. (i) Volume transport by class, plotted directly as Sv rather than a percentage, with the same colour convention.

3.5 Internal-wave and double-diffusive mixing regimes

Vertical exchange was quantified across the four density-defined IOIs introduced above (σ_0 = 29.120, 29.184, 29.195 and 29.203 kg m^{-3}). The three deeper ones are drawn as black lines in Fig. 5: the OML top (29.184 kg m^{-3}), the OML base (29.195 kg m^{-3}), and the deep interface within the EMDW (29.203 kg m^{-3}). The shallowest lies between roughly 185 and 270 m across the transect, above the 450 m upper limit of the panels, and is therefore not shown. Profiles of σ_0, plotted as the anomaly $\Delta\sigma_0$ relative to its value at 450 m at each station, show that the three plotted interfaces are strongly deformed across the transect: all deepen from the western side toward the central stations and shoal again toward the east, indicating baroclinic tilting and lateral density gradients across the OML core. The deformation is strongest at the central-eastern stations, where the lowest-oxygen waters lie between the OML top and base (Fig. 5a), consistent with the oxygen section (Fig. 1d), and the density structure is locally disrupted near the OML boundaries, particularly where σ_0 exceeds 29.203 kg m^{-3}, marking sharp transitions between the low-oxygen core and the more ventilated waters above and below. The deep interface is crossed at four stations only; at ctd10, the deepest cast of the transect, σ_0 reaches a maximum of 29.201 kg m^{-3} near 2120 m and the interface is absent. The velocity cross-section (Fig. 5b) shows enhanced absolute velocities near the OML base and in the deeper layers, with localized maxima of 0.10–0.15 m s^{-1} along the central and eastern profiles and near the bottom. These jets are sheared over vertical scales of roughly 100–300 m and coincide with the density interfaces separating the OML from the waters below, supplying the shear that drives internal-wave mixing there.

The two diffusivities are complementary (Fig. 5c,d). K_ρ^{IW} is weakest within the OML core, dropping below about 10^{-5} m^2 s^{-1} at the OML top, and increases markedly at the lower boundary and in the deep layer beneath, reaching $10^{-3.5}$–10^{-3} m^2 s^{-1} in patches near 1200–1300 m that are co-located with the sheared jets. K_ρ^{DD} instead peaks near the upper OML boundary, where between about 600 and 1000 m several profiles display staircase-like density segments 25–50 m thick with $\Delta\sigma_0$ steps of about 2–3 × 10^{-3} kg m^{-3}; there K_ρ^{DD} remains about $10^{-4.5}$–10^{-4} m^2 s^{-1} even where K_ρ^{IW} weakens below 10^{-5} m^2 s^{-1}, so the upper OML interface is controlled by double diffusion rather than by internal-wave mixing.

The frequency distribution of the diffusivity estimates (Fig. S3) confirms this partitioning. The internal-wave diffusivities (IW) peak near $10^{-5.2}$ m^2 s^{-1} with a secondary mode around $10^{-3.7}$ m^2 s^{-1} and a tail extending to $10^{-2.4}$ m^2 s^{-1}, consistent with their occurrence in the strongly sheared deep jets; the strain-based product (IW*) is narrower, confined to $10^{-6.6}$–$10^{-4.3}$ m^2 s^{-1}; and the double-diffusive diffusivities (DD) form a distinct mode near $10^{-3.9}$ m^2 s^{-1}, set mainly by the DD-active layers below the staircase region and about 1.3 orders of magnitude above the main IW mode. The two families overlap where internal-wave

https://doi.org/10.5194/egusphere-2026-6912
Preprint. Discussion started: 12 November 2026
© Author(s) 2026. CC BY 4.0 License.

mixing is strongest, the IW secondary mode and tail exceeding the DD mode, but their bulk distributions are offset and the two processes are active at different interfaces.

Overall, the mixing regime is vertically asymmetric: internal-wave diffusivities are enhanced at the OML base and the deeper interfaces, where shear is strongest, whereas double-diffusive diffusivities are more prominent near the upper OML boundary. This contrast, internal-wave-driven exchange below and a double-diffusive cap above, is the mechanistic basis for the asymmetric diffusive tracer fluxes described next.

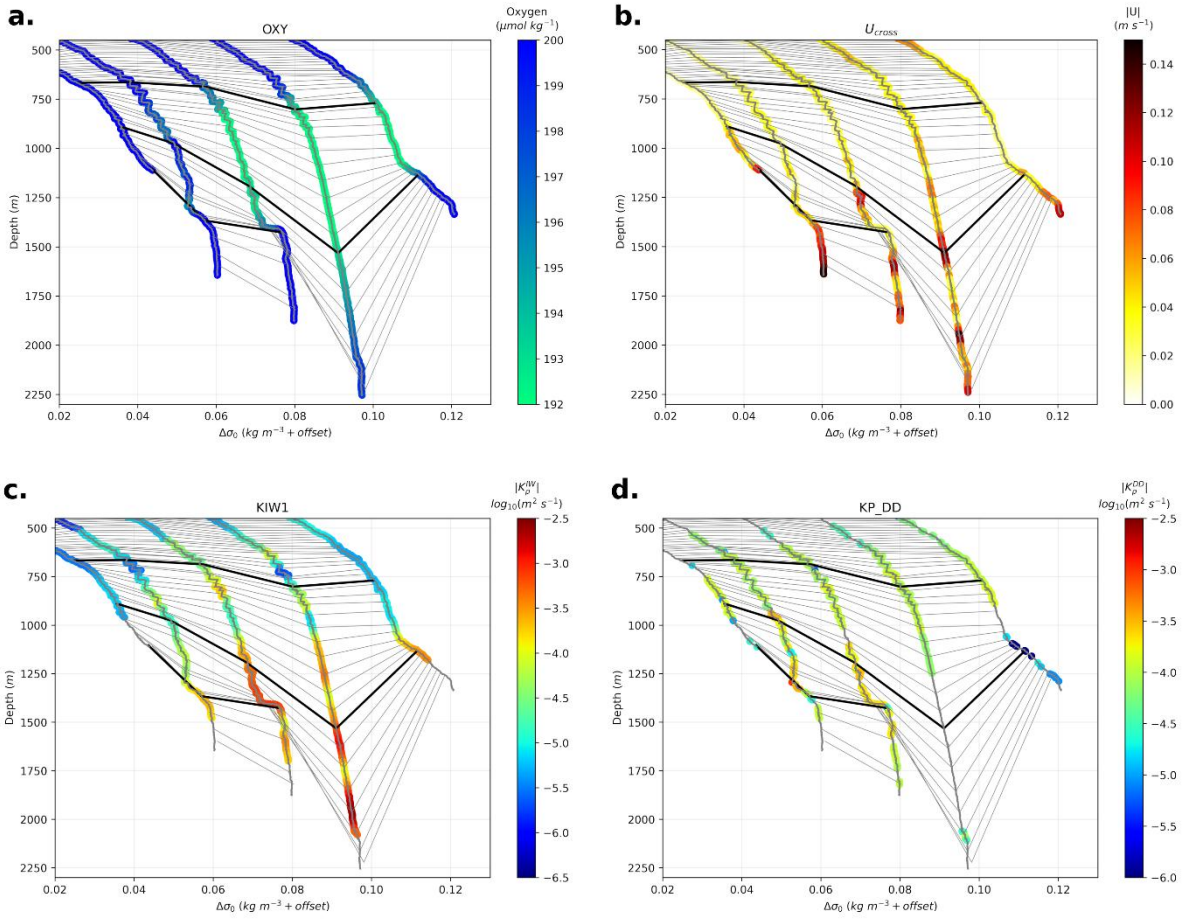


Figure 5: Vertical structure of density, oxygen, velocity, and turbulent diffusivity around the OML. Potential-density anomaly profiles (σ_0) are shown as $\Delta\sigma_0$ relative to the value at 450 m, set to zero for each station. Profiles from CTD06, CTD08, CTD09, CTD10, and CTD12 are displayed sequentially with a 0.02 kg m^{-3} horizontal offset for clarity. Grey lines indicate the mean depths of isopycnals between σ_0 = 29.150 and 29.225 kg m^{-3} at 0.001 kg m^{-3} intervals. Black lines mark the three deep IOIs. The panels span 450–2250 m to focus on the OML core and the adjacent deep interfaces. Coloured profiles show (a) dissolved oxygen (μmol kg^{-1}); (b) cross-section velocity magnitude |U| (m s^{-1}); (c) turbulent diffusivity Kρ from the internal-wave finescale parameterization (log$_{10}$ m^2 s^{-1}); and (d) turbulent diffusivity Kρ from the double-diffusive parameterization (log$_{10}$ m^2 s^{-1}; SF+ DD)

https://doi.org/10.5194/egusphere-2026-6912
Preprint. Discussion started: 12 November 2026
© Author(s) 2026. CC BY 4.0 License.

3.6 Diffusive tracer fluxes at key density interfaces

Vertical diffusive fluxes across the four IOIs reveal a strongly asymmetric pattern of property exchange around the OML and the underlying deep layers (Fig. 6, Table S1; positive = upward). All values, uncertainties, significance ratios and dominant processes are listed in Table S1. Fluxes are reported as the total (double-diffusion + internal-wave) flux ± 1u, in g m^{-2} s^{-1} for salinity and µmol m^{-2} s^{-1} for all other tracers, with $|F| \geq 2u$ taken as robust and 1–2u as marginal.

Salinity, oxygen, DIC and TA behave coherently at every interface and are treated here as a group. The grouping is not based on conservative behaviour: of the four, only salinity has no interior sources or sinks, whereas oxygen is consumed by respiration, DIC is produced by remineralization, and TA is modified by carbonate dissolution and, to a lesser degree, by nutrient cycling. That their fluxes nonetheless share a common vertical structure indicates that physical transport, rather than interior biogeochemical transformation, sets their vertical exchange across these interfaces.

Salinity, oxygen, DIC and TA are transferred upward at the two deeper interfaces and downward across the OML top, and the dominant process switches with them. At the deep interface (σ_0 = 29.203 kg m^{-3}) and at the OML base (σ_0 = 29.195 kg m^{-3}) the exchange is internal-wave-dominated: all four fluxes are robust at the deep interface, while at the OML base salinity, DIC and TA are robust and oxygen is upward but only marginal (1.9u). Across the OML top (σ_0 = 29.184 kg m^{-3}) the direction reverses and the exchange becomes double-diffusion-dominated, all four fluxes being robust. At the shallowest interface (σ_0 = 29.120 kg m^{-3}) only a small downward salinity flux is resolved, oxygen, DIC and TA are not significant, and magnitudes throughout are much smaller than at the OML boundaries and the deep interface.

Nutrients are decoupled from this pattern. Phosphate and silicic acid are robustly upward at the two shallowest interfaces and predominantly double-diffusion-dominated, silicic acid at the OML top carrying the largest upward flux of the section ($+2.16\times10^{-3} \pm 0.22\times10^{-3}$, 10.0u), but both reverse to robustly downward and internal-wave-driven at the deep interface, where silicic acid also has its strongest downward flux. Nitrate is negligible everywhere except for a marginal downward flux at the deep interface. The OML top therefore carries phosphate and silicic acid upward while salinity, oxygen, DIC and TA move downward. Because the double-diffusive flux is computed as $|K_\rho^{DD}|$ times the local gradient, these directions follow from the sign of the local gradients, oxygen, salinity, DIC and TA decreasing downward into the OML while phosphate and silicic acid increase, rather than from any tracer selectivity of the double-diffusive process itself.

Considering the OML as a layer bounded by its two interfaces, the oxygen fluxes converge into it, as expected for diffusion acting on an oxygen minimum: oxygen enters from above through the downward flux at the OML top (-1.54×10^{-2} µmol m^{-2} s^{-1}) and from below through the upward flux at the OML base ($+2.63\times10^{-2}$). The supply from below is roughly 1.7 times that from above, but the lower-boundary flux is itself only marginally resolved (1.9u), so the ratio indicates the direction of the asymmetry rather than a quantitative partition. The layer is thus diffusively ventilated preferentially from below, consistent with the enhanced internal-wave mixing at its base relative to the weaker, double-diffusion-dominated top. That the OML persists despite this two-sided diffusive oxygen input implies that in situ consumption and the advective import of low-oxygen water compensate for the diffusive supply.

https://doi.org/10.5194/egusphere-2026-6912
Preprint. Discussion started: 12 November 2026
© Author(s) 2026. CC BY 4.0 License.

One caveat applies to the deepest of these interfaces. Although σ_0 = 29.203 kg m^{-3} lies within the EMDW domain, EMDW-r and EMDW-ad share the same density range and are in lateral rather than density contact, so this interface quantifies diapycnal exchange between the waters above and below it, not exchange between the two deep classes.

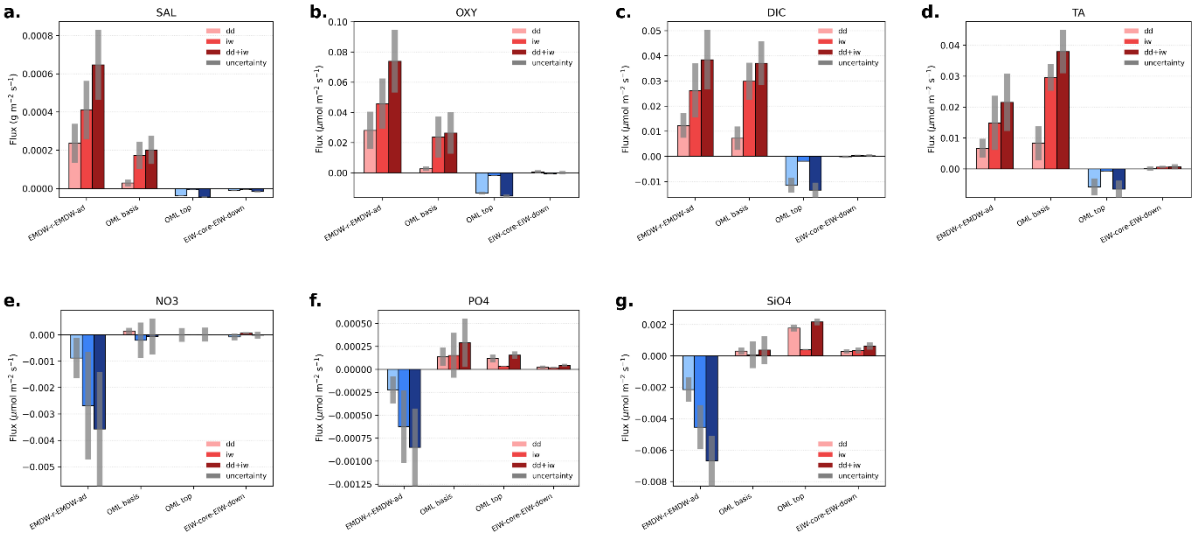


Figure 6: Vertical tracer fluxes estimate across σ0=29.120 kg m^{-3} (EIW-core-EIW-down), 29.184 kg m^{-3} (OML top), 29.195 kg m^{-3} (OML base), and 29.203 kg m^{-3} (deep interface within the EMDW). Light, intermediate, and dark bars show the Kiw , Kdd, and combined estimates, respectively. Positive values, shown in red, indicate upward fluxes; negative values, shown in blue, indicate downward fluxes. $K_{iw}K_{dd}$.

4 Discussion

4.1 Physical setting and cyclonic forcing

The results indicate cyclonic circulation at the Gulf entrance in December 2023. The principal observational evidence is the central sea-level depression, counter-clockwise surface current field, isopycnal doming, and opposing eastern and western transport branches. These data establish the circulation state but do not determine whether local wind forcing generated, intensified, or merely coincided with the gyre.

The isopycnal dome displaced the nutrient and DIC gradients upward between approximately 17.6°E and 18.0°E. This reduced the vertical distance between the upper layer and subsurface tracer reservoirs. Whether that displacement enhances euphotic-zone nutrient supply or productivity cannot be determined without vertical velocity, light, chlorophyll, or production measurements; satellite chlorophyll in the Gulf is known to vary strongly on seasonal and interannual timescales (Ciancia et al., 2018).

The branch transports show an exchange geometry rather than a closed budget. ISW/AW-e was the only consistently resolved positive branch; EMDW-r was positive but generally marginal; the western surface, EIW-core and EIW-down contributions

https://doi.org/10.5194/egusphere-2026-6912
Preprint. Discussion started: 12 November 2026
© Author(s) 2026. CC BY 4.0 License.

were negative; and EMDW-ad was not resolved in either direction, consistent with a through-flowing vein whose eastern inflow and western outflow cancel in the section integral. The largest positive nutrient contribution was associated with EMDW-r, but exceeds its own uncertainty by a factor of 1.4–1.8 marginal by the criterion adopted under Water-mass classes and tracer fluxes calculations, and the section integrated transport is itself unresolved, so it cannot be described as the principal or persistent external nutrient source.

The intermediate and deep properties should also be interpreted within the recent regional warming and salinization documented by Terzić et al. (2025), Terzić and Vilibić (2026) and Menna et al. (2026). The PIONEER-2023 section is compatible with this evolving background, but no trend can be inferred from one snapshot. Repeat sections are required to distinguish regional thermohaline change from local gyre displacement and mesoscale variability.

The deep velocity structure suggests a connected pathway. The strongest inflow core below 800 m lies near 1350 m on the eastern flank (+0.11 m s^{-1}), and the strongest outflow core near 1640 m on the western flank (−0.14 m s^{-1}), about 300 m deeper. Both features have counterparts in the SA fields and in the CT isolines, consistent with Adriatic-derived dense water entering from the east and deepening as it circulates through the Gulf before leaving on the western side. Such a pathway would be consistent with the transformation mechanism proposed by Sellschopp and Álvarez (2003), although a single transect cannot establish continuity between the two features.

4.2 Vertically asymmetric exchange around the OML

The OML was bounded by different parameterized mixing regimes. Here, "ventilation" refers narrowly to oxygen transfer from surrounding, more oxygenated water into the OML; it is not used as a direct estimate of water-mass age or formation rate. The lower boundary coincided with sheared deep veins and locally elevated KρIW, whereas the upper boundary contained layered hydrographic structure and elevated KρDD. This vertical contrast is supported by the relative distribution of the parameterized estimates, although neither process was measured directly with microstructure instruments. The elevated deep internal-wave diffusivities occur over the steep flanks of the section, where topographic generation is plausible (Ceramicola et al., 2024; Musgrave et al., 2022); the present transect resolves neither the generation sites nor the wave field, so this remains a hypothesis. Several structural terms condition this result, and none of them enters the propagated and bootstrap errors reported under Diffusive tracer fluxes at key density interfaces. On the diffusivity side these are the factor-of-three adjustment to KρIW, the sample-dependent Rρ masks, the restriction of the flux calculation to double-diffusively active patches, and the use of a single effective KρDD for chemically distinct tracers (see Diffusive vertical fluxes). A further and potentially larger term affects the deep internal-wave estimates specifically: the secondary diffusivity mode is associated with jets sheared over vertical scales of 100–300 m, and where that shear is sub-inertial rather than wave-borne the shear–strain parameterization overestimates dissipation (Takahashi and Hibiya, 2019); no spectral saturation cutoff was applied here to limit this effect. The upward salt, oxygen and carbonate-system fluxes at the OML base and at the deep interface, which are internal-wave-dominated and co-located with these jets, should therefore be read as upper bounds. On the gradient side, the fluxes of the

https://doi.org/10.5194/egusphere-2026-6912
Preprint. Discussion started: 12 November 2026
© Author(s) 2026. CC BY 4.0 License.

bottle-sampled tracers rest on discrete profiles interpolated onto the 1 m grid, so their reported significance reflects the interpolated gradients rather than the discrete sampling. Taken together, the mixing results are best treated as hypotheses about relative process dominance and flux direction, not as rates.

Within that framework, the oxygen-flux directions are physically coherent with an oxygen minimum: the upward estimate at the base and the downward estimate at the top both point into the OML. Diffusion alone would weaken the oxygen minimum rather than maintain it. If the observed OML were approximately steady over times longer than the survey, its persistence would require compensating oxygen sinks or transport terms. Candidate terms include respiration and remineralization within the layer, along-isopycnal import of low-oxygen water, and temporal changes in the position or thickness of the OML. The present data do not quantify those terms. Consequently, the statement that consumption and low-oxygen advection compensate for the diffusive input is a budget hypothesis, not an observational result. The ratio of approximately 1.7 between the lower- and upper-boundary oxygen fluxes describes the parameterized snapshot only, and rests on a lower-boundary flux that is itself only marginally resolved (1.9u). Lateral structure is also important. The section oxygen minimum and AOU maximum both lie within the OML near 1010 m at 17.80°E (see Dissolved oxygen and apparent oxygen utilization), whereas the western side remained better oxygenated at comparable depths. Plausible explanations include along-isopycnal advection, western boundary exchange, mesoscale displacement, or connection with shallower oxygenated water; the section does not discriminate among them.

The OML should therefore be interpreted as a three-dimensional feature shaped by lateral water-mass geometry and biogeochemical oxygen demand as well as by diapycnal exchange. A closed OML oxygen budget would require repeated hydrography, direct turbulence measurements, estimates of biological oxygen consumption, and observations or modelling of along-isopycnal transport.

4.3 Biogeochemical expression of circulation and renewal

Nutrient, oxygen, AOU, DIC, and TA fields show that the biogeochemical properties cannot be explained by depth alone. Isopycnal displacement, lateral water-mass contrasts, oxygen utilization, and mixing all contribute, with the clearest convergence of signals in the central-eastern OML.

Near-surface nutrient depletion is consistent with the oligotrophic regional setting, while the shoaling of nutrient isolines follows the cyclonic hydrography. Because the bottle samples are sparse and objectively mapped, the apparent vertical gradients should be interpreted at the resolved section scale rather than as a fine vertical structure. Nitrate, phosphate, and silicic acid had different deep distributions. Nitrate formed a broad mid-depth maximum, silicic acid accumulated most strongly in the deeper central-eastern layer, and phosphate showed the closest spatial correspondence with the AOU maximum.

https://doi.org/10.5194/egusphere-2026-6912
Preprint. Discussion started: 12 November 2026
© Author(s) 2026. CC BY 4.0 License.

These contrasts are compatible with differing regeneration, and source-water histories, but the present data do not quantify individual process rates.

Alternative explanations include lateral import of preconditioned nutrient signatures, different residence times among the classes, and interpolation across sparsely sampled deep layers. The nutrient maxima should therefore not be attributed solely to local remineralization. The cyclonic state sampled here shortens the vertical distance between the upper layer and the subsurface nutrient reservoir; under the opposite gyre polarity the same isopycnals would be depressed and that separation would increase. Whether the diffusive nutrient fluxes reported here would respond cannot be tested from a single survey, and we raise it as a hypothesis for repeat sampling in both circulation states. Consistent with this, the largest positive nutrient transport in the section was carried by EMDW-r rather than by the Adriatic-derived vein (see Tracer transports across the section), so the deep nutrient signal is associated with the resident inflow rather than with recent Adriatic renewal, although that transport is itself only marginally resolved.

The vertical-flux estimates reinforce the absence of a single nutrient pathway: phosphate and silicic acid were upward at the shallower interfaces, whereas their deepest-interface estimates were downward, and nitrate was mostly unresolved. These results are conditional on the effective-diffusivity assumption and the unresolved section aggregation.

AOU integrates oxygen saturation disequilibrium, subsequent respiration, and mixing. Its maximum within the OML, together with low oxygen and elevated phosphate and silicic acid, identifies the water with the greatest oxygen deficit and regenerated-nutrient signature sampled on the transect. It does not establish that this water is the oldest or that the observed AOU was generated locally.

DIC and TA provide complementary but non-unique information. DIC followed the uplifted intermediate layers and increased with AOU over a limited upper-water range, but the deep classes departed from that trend. TA had weaker vertical gradients and a non-significant section-wide relationship with SA.

The flat TA–SA regression reflects the depth-ordered organization of alkalinity among the classes rather than a single mixing line, including Adriatic-influenced and open-Mediterranean waters. It is not sufficient evidence for a specific two-endmember model, nor does it exclude localized coastal alkalinity inputs.

Similarly, the low DIC at high-AOU deep samples points to differences in source-water and preformed properties. The direction of the offset is consistent with rising atmospheric CO_2, because water ventilated earlier would generally carry a “low preformed DIC”. Its magnitude, however, is not independently constrained. A reconciliation of the carbon- and thermohaline-based age estimates, which agree in sign but differ by a factor of two to three, is given in Sect. S1 of the Supplement; the inferred timescales should be read as qualitative age equivalents rather than as dated water masses.

https://doi.org/10.5194/egusphere-2026-6912
Preprint. Discussion started: 12 November 2026
© Author(s) 2026. CC BY 4.0 License.

The observations show close juxtaposition of surface, intermediate, transitional, and deep regimes at the Gulf entrance during a cyclonic state. They support a conceptual model in which lateral exchange and isopycnal displacement set the large-scale tracer geometry, while parameterized diapycnal processes redistribute properties at selected interfaces. They do not demonstrate a long-term transformation rate or a net Gulf-scale biogeochemical source or sink.

5 Conclusions

The PIONEER-2023 observations provide a full-depth view of the coupled physical and biogeochemical structure at the entrance of the Gulf of Taranto during late November–early December 2023. A basin-scale cyclonic gyre, associated with strong isopycnal doming and the uplift of nutrient-rich subsurface waters, organizes the distribution of water masses, oxygen, nutrients, and carbonate-system properties across the entrance of the Gulf.

Water-mass analysis revealed a vertically and laterally structured exchange system linking Adriatic-influenced surface waters, Eastern Intermediate Water and its weakly ventilated lower part, a pronounced OML near 1000 m, 'resident' deep waters and Adriatic-derived deep intrusions. Transport estimates highlighted an asymmetric inflow–outflow circulation in which a robust eastern surface inflow and a weaker, marginally resolved, deep Adriatic renewal branch were compensated by exports in surface and intermediate layers. Although net section-integrated tracer budgets were not distinguishable from zero within uncertainty, the observations clearly resolved the partitioning of exchange among the different water-mass classes.

The OML emerged as the central biogeochemical feature of the system. Its boundaries were characterized by contrasting parameterized mixing regimes: double-diffusive processes dominated near the upper interface, while enhanced internal-wave turbulence was concentrated at its lower boundary and within deeper sheared layers. This vertical asymmetry resulted in distinct pathways of tracer exchange across density interfaces. Oxygen, dissolved inorganic carbon, and alkalinity were preferentially supplied from below through internal-wave-driven mixing, although each also entered across the upper interface, so that the diffusive fluxes converge into the layer from both sides, whereas nutrient fluxes displayed tracer-specific behaviour and responded differently to the competing influence of double diffusion and turbulence. The carbonate system was not organized like oxygen and the nutrients: the deep classes departed from the upper-water relationship between DIC and apparent oxygen utilization, and alkalinity showed no detectable section-wide relationship with salinity, indicating that interior carbonate properties reflect source-water provenance and preformed composition rather than a single remineralization pathway.

Taken together, these results show that the Gulf of Taranto functions as an active transformation zone rather than a passive conduit between the Adriatic and Ionian Seas. Cyclonic circulation establishes the large-scale architecture of water masses and tracer distributions, while vertically contrasting mixing processes regulate the redistribution of oxygen, nutrients, and carbon across the water column.

These mechanisms together shape the OML. Because oxygen is transferred into the OML across both of its boundaries, the parameterized diapycnal fluxes act to erode rather than to sustain the minimum; its persistence therefore requires consumption

https://doi.org/10.5194/egusphere-2026-6912
Preprint. Discussion started: 12 November 2026
© Author(s) 2026. CC BY 4.0 License.

or advective terms that the present design does not resolve. The same mixing contrast nonetheless modulates biogeochemical exchange between the Gulf and the broader Ionian Sea. These conclusions rest on a single snapshot and on parameterized rather than measured mixing, with sparse deep bottle coverage and dissolved inorganic carbon derived from pH and alkalinity rather than measured independently.

More broadly, our findings suggest that future changes in circulation, stratification, or Adriatic deep-water renewal may alter both water-mass pathways and the efficiency of oxygenation and nutrient transfer in this key Mediterranean transition region. Repeated sampling, direct microstructure observations, and integrated physical–biogeochemical monitoring will therefore be essential to determine how persistent the observed exchange regime is and how it may evolve under ongoing climatic and thermohaline change.

Code and data availability

The dataset supporting this study has been submitted to PANGAEA and is undergoing editorial processing. The DOI will be provided to the journal as soon as it is issued.

Supplement

Sect. S1: Water-mass ages and preformed carbon.

Table S1. Combined (double-diffusion + internal-wave) vertical diffusive tracer fluxes across the four interfaces of interest.

Fig. S1. Atmospheric forcing and hydrographic context.

Fig. S2. Carbonate-system property–property relationships for discrete bottle samples, coloured by hydrographic-biogeochemical class.

Fig. S3. Frequency distributions of parameterized vertical diffusivity.

Author contributions

Malek Belgacem and Florian V. M. Kokoszka: Conceptualization; Formal analysis; Investigation; Visualization; Writing – original draft; Writing – review and editing; Funding acquisition. Carolina Cantoni: Investigation; Validation; Writing – review and editing. Katrin Schroeder: Investigation; Supervision; Writing – review and editing. Jacopo Chiggiato: Investigation;

https://doi.org/10.5194/egusphere-2026-6912
Preprint. Discussion started: 12 November 2026
© Author(s) 2026. CC BY 4.0 License.

Writing – review and editing. Stefania Sparnocchia: Investigation; Writing – review and editing. Elena Fragiacomo: Investigation. Francesco Acri: Investigation. Marzia Rovere: Project administration; Resources; Investigation.

Competing interests

None declared.

Acknowledgements

We thank Lorenzo Consorti for sample collection. Data were collected during PIONEER-2023, a CNR initiative and the first scientific expedition of R/V Gaia Blu. This study used EU Copernicus Marine Service information. AI-assisted tools were used for grammar editing; the authors reviewed and approved the text.

Financial support

Malek Belgacem's and Elena Fragiacomo's fellowships were supported by EU EuroGO-SHIP (grant 101094690). Florian Kokoszka's research grant was funded by EU NextGenerationEU (PRIN/PNRR), ITINERIS (IR0000032).

References

Álvarez, M., Sanleón-Bartolomé, H., Tanhua, T., et al.: The CO_2 system in the Mediterranean Sea: a basin-wide perspective, Ocean Sci., 10, 69–92, https://doi.org/10.5194/os-10-69-2014, 2014.

Anderson, L. A. and Sarmiento, J. L.: Redfield ratios of remineralization determined by nutrient data analysis, Global Biogeochem. Cycles, 8, 65–80, https://doi.org/10.1029/93GB03318, 1994.

Artegiani, A., Bregant, D., Paschini, E., Pinardi, N., Raicich, F., and Russo, A.: The Adriatic Sea general circulation, Part I: Air–sea interactions and water mass structure. J. Phys. Oceanogr., 27, 1492–1514, https://doi.org/10.1175/1520-0485(1997)027<1492:TASGCP>2.0.CO;2, 1997a.

Artegiani, A., Bregant, D., Paschini, E., Pinardi, N., Raicich, F., and Russo, A.: The Adriatic Sea general circulation, Part II: Baroclinic circulation structure. J. Phys. Oceanogr., 27, 1515–1532, https://doi.org/10.1175/1520-0485(1997)027<1515:TASGCP>2.0.CO;2, 1997b.

https://doi.org/10.5194/egusphere-2026-6912
Preprint. Discussion started: 12 November 2026
© Author(s) 2026. CC BY 4.0 License.

Borzelli, G. L. E., Gačić, M., Cardin, V., and Civitarese, G.: Eastern Mediterranean Transient and reversal of the Ionian Sea circulation, Geophys. Res. Lett., 36, L15108, https://doi.org/10.1029/2009GL039261, 2009.

Bretherton, F. P., Davis, R. E., and Fandry, C. B.: A technique for objective analysis and design of oceanographic experiments applied to MODE-73, Deep-Sea Res. Oceanogr. Abstr., 23, 559–582, https://doi.org/10.1016/0011-7471(76)90001-2, 1976.

Budillon, G., Lo Bue, N., Siena, G., and Spezie, G.: Hydrographic characteristics of water masses and circulation in the Northern Ionian Sea, Deep-Sea Res. Part II, 57, 441–457, https://doi.org/10.1016/j.dsr2.2009.08.017, 2010.

Cantoni, C., Luchetta, A., Celio, M., Cozzi, S., Raicich, F., and Catalano, G.: Carbonate system variability in the Gulf of Trieste (North Adriatic Sea), Estuar. Coast. Shelf Sci., 115, 51–62, https://doi.org/10.1016/j.ecss.2012.07.006, 2012.

Cantoni, C., De Vittor, C., Faganeli, J., et al.: Carbonate system and acidification of the Adriatic Sea, Mar. Chem., 267, 104462, https://doi.org/10.1016/j.marchem.2024.104462, 2024.

Ceramicola, S., Senatore, M. R., Cova, A., et al.: Geohazard features of the Gulf of Taranto, J. Maps, 20, 2431073, https://doi.org/10.1080/17445647.2024.2431073, 2024.

Ciancia, E., Coviello, I., Di Polito, C., et al.: Investigating the chlorophyll-a variability in the Gulf of Taranto (North-western Ionian Sea) by a multi-temporal analysis of MODIS-Aqua Level 3/Level 2 data, Cont. Shelf Res., 155, 34–44, https://doi.org/10.1016/j.csr.2018.01.011, 2018.

Civitarese, G., Gačić, M., Lipizer, M., and Eusebi Borzelli, G. L.: On the impact of the Bimodal Oscillating System (BiOS) on the biogeochemistry and biology of the Adriatic and Ionian Seas, Eastern Mediterranean, Biogeosciences, 7, 3987–3997, https://doi.org/10.5194/bg-7-3987-2010, 2010.

Copin-Montégut, C.: Alkalinity and carbon budgets in the Mediterranean Sea, Global Biogeochem. Cycles, 7, 915–925, https://doi.org/10.1029/93GB01826, 1993.

Davis, R. E.: Objective mapping by least squares fitting, J. Geophys. Res., 90, 4773–4777, https://doi.org/10.1029/JC090iC03p04773, 1985.

Dickson, A. G.: Standard potential of the reaction AgCl(s) + ½H_2(g) = Ag(s) + HCl(aq), and the standard acidity constant of the ion HSO_4^- in synthetic seawater from 273.15 to 318, 15 K. J. Chem. Thermodyn., 22, 113–127, https://doi.org/10.1016/0021-9614(90)90074-Z, 1990.

https://doi.org/10.5194/egusphere-2026-6912
Preprint. Discussion started: 12 November 2026
© Author(s) 2026. CC BY 4.0 License.

Dickson, A. G., Sabine, C. L., and Christian, J. R. (Eds.): Guide to best practices for ocean CO_2 measurements, PICES Special Publication 3. North Pacific Marine Science Organization, 2007.

D'Ortenzio, F. and Ribera d'Alcalà, M.: On the trophic regimes of the Mediterranean Sea: a satellite analysis, Biogeosciences, 6, 139–148, https://doi.org/10.5194/bg-6-139-2009, 2009.

Emery, W. J. and Thomson, R. E.: Data analysis methods in physical oceanography, Pergamon, 1997.

Federico, I., Pinardi, N., Coppini, G., Oddo, P., Lecci, R., and Mossa, M.: Coastal ocean forecasting with an unstructured-grid model in the southern Adriatic and northern Ionian seas, Nat. Hazards Earth Syst. Sci., 17, 45–59, https://doi.org/10.5194/nhess-17-45-2017, 2017.

Federico, I., Pinardi, N., Lyubartsev, V., et al.: Observational evidence of the basin-wide gyre reversal in the Gulf of Taranto, Geophys. Res. Lett., 47, e2020GL091030, https://doi.org/10.1029/2020GL091030, 2020.

Ferron, B., Kokoszka, F., Mercier, H., and Lherminier, P.: Dissipation rate estimates from microstructure and finescale internal wave observations along the A25 Greenland–Portugal OVIDE section, J. Atmos. Oceanic Technol., 31, 2530–2543, https://doi.org/10.1175/JTECH-D-14-00036.1, 2014.

Fine, E. C., Alford, M. H., MacKinnon, J. A., and Mickett, J. B.: Microstructure mixing observations and finescale parameterizations in the Beaufort Sea, J. Phys. Oceanogr., 51, 19–35, https://doi.org/10.1175/JPO-D-19-0233.1, 2021.

Gelb, A. (Ed.): Applied optimal estimation, MIT Press, 1974.

Grasshoff, K., Kremling, K., and Ehrhardt, M. (Eds.): Methods of seawater analysis, 3rd ed, Wiley-VCH, 1999.

Gregg, M. C.: Scaling turbulent dissipation in the thermocline, J. Geophys. Res., 94, 9686–9698, https://doi.org/10.1029/JC094iC07p09686, 1989.

Guarnieri, A., Pinardi, N., Oddo, P., Bortoluzzi, G., and Ravaioli, M.: Impact of tides in a baroclinic circulation model of the Adriatic Sea, J. Geophys. Res. Oceans, 118, 166–183, https://doi.org/10.1029/2012JC007921, 2013.

Hansen, H. P. and Koroleff, F.: Determination of nutrients, in: Methods of seawater analysis, 3rd edn., edited by: Grasshoff, K., Kremling, K., and Ehrhardt, M., Wiley-VCH, 159–228, 1999.

Hernández-Ayón, J. M., Belli, S. L., and Zirino, A.: pH, alkalinity and total CO_2 in coastal seawater by potentiometric titration with a difference derivative readout, Anal. Chim. Acta, 394, 101–111, https://doi.org/10.1016/S0003-2670(99)00207-3, 1999.

https://doi.org/10.5194/egusphere-2026-6912
Preprint. Discussion started: 12 November 2026
© Author(s) 2026. CC BY 4.0 License.

Hiller, W. and Käse, R. H.: Objective analysis of hydrographic data sets from mesoscale surveys, Ber. Inst. Meereskd. Christian-Albrechts-Univ. Kiel, 116, 1–78, 1983.

Ingrosso, G., Giani, M., Comici, C., et al.: Drivers of the carbonate system seasonal variations in a Mediterranean gulf, Estuar. Coast. Shelf Sci., 168, 58–70, https://doi.org/10.1016/j.ecss.2015.11.001, 2016.

Inoue, R., Yamazaki, H., Wolk, F., Kono, T., and Yoshida, J.: An estimation of buoyancy flux for a mixture of turbulence and double diffusion, J. Phys. Oceanogr., 37, 611–624, https://doi.org/10.1175/JPO2996.1, 2007.

Kamen, E. W. and Su, J. K.: Introduction to optimal estimation, Springer, 1999.

Kokoszka, F., Iudicone, D., Zingone, A., Saggiomo, V., Ribera d'Alcalà, M., and Conversano, F.: A note about density staircases in the Gulf of Naples: 20 years of persistent weak salt-fingering layers in a coastal area, Adv. Oceanogr. Limnol., 12, 10008, https://doi.org/10.4081/aiol.2021.10008, 2021.

Kokoszka, F., Sparnocchia, S., Cavaliere, D., et al.: Bottom topography effects on the internal wave climate in the Ionian Sea, Ocean Sci., 22, 2249–2265, https://doi.org/10.5194/os-22-2249-2026, 2026.

Kunze, E., Firing, E., Hummon, J. M., Chereskin, T. K., and Thurnherr, A. M.: Global abyssal mixing inferred from lowered ADCP shear and CTD strain profiles, J. Phys. Oceanogr., 36, 1553–1576, https://doi.org/10.1175/JPO2926.1, 2006.

Lewis, E. and Wallace, D. W. R.: Program developed for CO_2 system calculations, ORNL/CDIAC-105. Carbon Dioxide Information Analysis Center, Oak Ridge National Laboratory, 1998.

Liebelt, P. B.: An introduction to optimal estimation, Addison-Wesley, 1967.

Liu, X., Patsavas, M. C., and Byrne, R. H.: Purification and characterization of meta-cresol purple for spectrophotometric seawater pH measurements, Environ. Sci. Technol., 45, 4862–4868, https://doi.org/10.1021/es200665d, 2011.

Lueker, T. J., Dickson, A. G., and Keeling, C. D.: Ocean pCO_2 calculated from dissolved inorganic carbon, alkalinity, and equations for K_1 and K_2: validation based on laboratory measurements of CO_2 in gas and seawater at equilibrium, Mar. Chem., 70, 105–119, https://doi.org/10.1016/S0304-4203(00)00022-0, 2000.

Manca, B. B., Ibello, V., Pacciaroni, M., Scarazzato, P., and Giorgetti, A.: Ventilation of deep waters in the Adriatic and Ionian Seas following changes in thermohaline circulation of the Eastern Mediterranean, Clim. Res., 31, 239–256, https://doi.org/10.3354/cr031239, 2006.

McDougall, T. J. and Barker, P. M.: Getting started with TEOS-10 and the Gibbs Seawater (GSW) Oceanographic Toolbox, SCOR/IAPSO WG127, 2011.

https://doi.org/10.5194/egusphere-2026-6912
Preprint. Discussion started: 12 November 2026
© Author(s) 2026. CC BY 4.0 License.

Menna, M., Gačić, M., Pirro, A., et al.: Salinity-driven dynamics in the central Mediterranean in the era of ocean warming, Environ. Res. Commun., 8, 045002, https://doi.org/10.1088/2515-7620/ae558a, 2026.

Musgrave, R. C., Pollmann, F., Kelly, S., and Nikurashin, M.: The lifecycle of topographically generated internal waves, in: Ocean mixing: drivers, mechanisms and impacts, edited by: Naveira Garabato, A. C. and Meredith, M., Elsevier, 117–144, https://doi.org/10.1016/B978-0-12-821512-8.00013-X, 2022.

Nakano, H. and Yoshida, J.: A note on estimating eddy diffusivity for oceanic double-diffusive convection, J. Oceanogr., 75, 375–393, https://doi.org/10.1007/s10872-019-00514-9, 2019.

Osborn, T. R.: Estimates of the local rate of vertical diffusion from dissipation measurements, J. Phys. Oceanogr., 10, 83–89, https://doi.org/10.1175/1520-0485(1980)010<0083:EOTLRO>2.0.CO;2, 1980.

Pérez, F. F. and Fraga, F.: Association constant of fluoride and hydrogen ions in seawater, Mar. Chem., 21, 161–168, https://doi.org/10.1016/0304-4203(87)90036-3, 1987.

Pinardi, N., Lyubartsev, V., Cardellicchio, N., et al.: Marine Rapid Environmental Assessment in the Gulf of Taranto: a multiscale approach, Nat. Hazards Earth Syst. Sci., 16, 2623–2639, https://doi.org/10.5194/nhess-16-2623-2016, 2016.

Polzin, K. L., Toole, J. M., and Schmitt, R. W.: Finescale parameterizations of turbulent dissipation, J. Phys. Oceanogr., 25, 306–328, https://doi.org/10.1175/1520-0485(1995)025<0306:FPOTD>2.0.CO;2, 1995.

Polzin, K. L., Naveira Garabato, A. C., Huussen, T. N., Sloyan, B. M., and Waterman, S.: Finescale parameterizations of turbulent dissipation, J. Geophys. Res. Oceans, 119, 1383–1419, https://doi.org/10.1002/2013JC008979, 2014.

Radko, T. and Smith, D. P.: Equilibrium transport in double-diffusive convection, J. Fluid Mech., 692, 5–27, https://doi.org/10.1017/jfm.2011.482, 2012.

Redfield, A. C., Ketchum, B. H., and Richards, F. A.: The influence of organisms on the composition of sea-water, in: The sea, v. 2, edited by: Hill, M. N., Wiley, 26–77, 1963.

Roether, W., Manca, B. B., Klein, B., et al.: Recent changes in Eastern Mediterranean deep waters, Science, 271, 333–335, https://doi.org/10.1126/science.271.5247.333, 1996.

Roether, W., Klein, B., Manca, B. B., Theocharis, A., and Kioroglou, S.: Transient Eastern Mediterranean deep waters in response to the massive dense-water output of the Aegean Sea in the 1990s, Prog. Oceanogr., 74, 540–571, https://doi.org/10.1016/j.pocean.2007.03.001, 2007.

https://doi.org/10.5194/egusphere-2026-6912
Preprint. Discussion started: 12 November 2026
© Author(s) 2026. CC BY 4.0 License.

Rovere, M., Falcini, F., Polonia, A., Schroeder, K., et al.: R/V Gaia Blu cruise report no, 1: PIONEER—Processes in the IONian Sea: Exploring, Experimenting, Researching. Rapporto Tecnico ISMAR-CNR 26. Istituto di Scienze Marine, Consiglio Nazionale delle Ricerche, https://doi.org/10.26383/CNR-ISMAR.2024.2, 2024.

Rubino, A., Falcini, F., Zanchettin, D., et al.: Abyssal undular vortices in the Eastern Mediterranean basin, Nat. Commun., 3, 834, https://doi.org/10.1038/ncomms1836, 2012.

Schneider, A., Wallace, D. W. R., and Körtzinger, A.: Alkalinity of the Mediterranean Sea, Geophys. Res. Lett., 34, L15608, https://doi.org/10.1029/2006GL028842, 2007.

Schroeder, K., Ben Ismail, S., Bensi, M., et al.: A consensus-based, revised and comprehensive catalogue for Mediterranean water masses acronyms, Mediterr. Mar. Sci., 25, 783–791, https://doi.org/10.12681/mms.38736, 2024.

Sellschopp, J. and Álvarez, A.: Dense low-salinity outflow from the Adriatic Sea under mild (2001) and strong (1999) winter conditions, J. Geophys. Res. Oceans 108(C9): 8104, https://doi.org/10.1029/2002JC001562, 2003.

Sellschopp, J. and Onken, R.: Lenses of extremely cold water in the central Ionian Sea, Oceanol. Acta, 23, 117–128, https://doi.org/10.1016/S0399-1784(00)00123-7, 2000.

Takahashi, A. and Hibiya, T.: Assessment of finescale parameterizations of deep ocean mixing in the presence of geostrophic current shear: results of microstructure measurements in the Antarctic Circumpolar Current region, J. Geophys. Res. Oceans, 124, 135–153, https://doi.org/10.1029/2018JC014030, 2019.

Takahashi, A. and Hibiya, T.: Influence of the distortion of vertical wavenumber spectra on estimates of turbulent dissipation using the finescale parameterization: observations in the Antarctic Circumpolar Current, J. Geophys. Res. Oceans, 126, e2020JC016613, https://doi.org/10.1029/2020JC016613, 2021.

Terzić, E. and Vilibić, I.: Twenty-first century thermohaline trends and abrupt shifts in the Ionian Sea, Front. Mar. Sci., 12, 1718186, https://doi.org/10.3389/fmars.2025.1718186, 2026.

Terzić, E., Cardin, V., Le Meur, J., Dunić, N., Vodopivec, M., and Vilibić, I.: Unprecedented warming and salinization observed in the deep Adriatic, Limnol. Oceanogr. Lett., 10, 888–898, https://doi.org/10.1002/lol2.70051, 2025.

Theocharis, A., Klein, B., Nittis, K., and Roether, W.: Evolution and status of the Eastern Mediterranean Transient, 1997–1999, J. Mar. Syst. 33–34: 91–116, https://doi.org/10.1016/S0924-7963(02)00054-4, 2002.

https://doi.org/10.5194/egusphere-2026-6912
Preprint. Discussion started: 12 November 2026
© Author(s) 2026. CC BY 4.0 License.



Trotta, F., Pinardi, N., Fenu, E., and Grandi, A.: Multi-nest high-resolution model of submesoscale circulation features in the Gulf of Taranto, Ocean Dyn., 67, 1609–1625, https://doi.org/10.1007/s10236-017-1110-z, 2017.

Turner, J. S.: Buoyancy effects in fluids, Cambridge Univ. Press, 1973.

Uppström, L. R.: The boron/chlorinity ratio of deep-sea water from the Pacific Ocean, Deep-Sea Res. Oceanogr. Abstr., 21, 161–162, https://doi.org/10.1016/0011-7471(74)90074-6, 1974.

Van Heuven, S., Pierrot, D., Rae, J. W. B., Lewis, E., and Wallace, D. W. R.: MATLAB program developed for CO_2 system calculations, ORNL/CDIAC-105b. Carbon Dioxide Information Analysis Center, Oak Ridge National Laboratory, https://doi.org/10.3334/CDIAC/otg.CO2SYS_MATLAB_v1.1, 2011.

Wunsch, C.: The ocean circulation inverse problem, Cambridge Univ. Press, 1996.

Zhang, J., Schmitt, R. W., and Huang, R. X.: Sensitivity of the GFDL Modular Ocean Model to parameterization of double-diffusive processes, J. Phys. Oceanogr., 28, 589–605, https://doi.org/10.1175/1520-0485(1998)028<0589:SOTGMO>2.0.CO;2, 1998.